A molecular switch controls assembly of bacterial focal adhesions

Bouchra Attia, Laetitia My, Jean Philippe Castaing, Céline Dinet, Hugo Le Guenno, Victoria Schmidt, Leon Espinosa, Vivek Anantharaman, L. Aravind, Corinne Sebban-Kreuzer, et al.

MICROBIOLOGY

A molecular switch controls assembly of bacterial focal adhesions

Bouchra Attia[1]†, Laetitia My[2]†, Jean Philippe Castaing[2], Céline Dinet[2], Hugo Le Guenno[3], Victoria Schmidt[1], Leon Espinosa[2], Vivek Anantharaman[4], L. Aravind[4], Corinne Sebban-Kreuzer[1], Matthieu Nouailler[1], Olivier Bornet[3], Patrick Viollier[5], Latifa Elantak[1]*, Tâm Mignot[2]*

Cell motility universally relies on spatial regulation of focal adhesion complexes (FAs) connecting the substrate to cellular motors. In bacterial FAs, the Adventurous gliding motility machinery (Agl-Glt) assembles at the leading cell pole following a Mutual gliding-motility protein (MglA)–guanosine 5′-triphosphate (GTP) gradient along the cell axis. Here, we show that GltJ, a machinery membrane protein, contains cytosolic motifs binding MglA-GTP and AglZ and recruiting the MreB cytoskeleton to initiate movement toward the lagging cell pole. In addition, MglA-GTP binding triggers a conformational shift in an adjacent GltJ zinc-finger domain, facilitating MglB recruitment near the lagging pole. This prompts GTP hydrolysis by MglA, leading to complex disassembly. The GltJ switch thus serves as a sensor for the MglA-GTP gradient, controlling FA activity spatially.

INTRODUCTION

Cell motility is central to all biological systems, from bacteria to animals, allowing adaptive responses and multicellular development. Eukaryotic cells move on surfaces via the formation of so-called focal adhesions, intracellular protein complexes where actin and myosin motors are recruited spatially to membrane-associated adhesion molecules (*1*). Eukaryotic focal adhesion complexes (eFAs) are regulated spatially by intricate signaling networks allowing cells to not only chemotax toward or away from chemical gradients but also respond directly to physical surfaces (*2*, *3*). eFA spatial assembly and dynamics are centrally regulated by small G proteins of the Ras-like superfamily (i.e., Rac, Rho, and Cdc42) regulating assembly, stability, and turnover of eFAs and promoting persistent cell migration in response to signals (*2*, *3*). Understanding the molecular details of these regulations is central to deciphering complex developmental and pathological processes, for example, the migration of immune cells during infection or the formation of metastasis during cancer.

Bacteria also move across surfaces using protein systems that are functionally equivalent to eFAs. For example, the predatory Gram-negative (diderm) bacterium *Myxococcus xanthus* moves by rotating along its long axis (Fig. 1A) (*4*) through a process called gliding motility (otherwise called A-motility). A-motility is powered by bacterial FAs (bFAs), which, analogous to the eFAs, contain a cytoskeletal motor and associated cell surface proteins [the so-called Adventurous gliding motility machinery–gliding transducer (Agl-Glt) complex] (*5*, *6*). Motile *Myxococcus* rod-shaped cells assemble motility motors at the cell pole (hence, the leading pole) that traffic helically in anticlockwise trajectories toward the lagging cell pole. When the motors interact with the underlying substrate via associated surface proteins, bFAs form and propel the clockwise screw–like movement of the cell (*4*). The molecular dynamics of bacterial proteins assembling at bFAs have been studied in detail and revealed several critical aspects of bFAs function:

1) The Agl-Glt system is a predicted multiprotein complex formed by at least 15 proteins localizing in all layers of the bacterial cell envelope (Fig. 1A) (*5*, *6*). At the core of this complex, the molecular motor consists of the three-protein AglR, AglQ, and AglS system (AglRQS), predicted to form a proton-conductive channel in the inner membrane (IM), similar to the TolQR complex in diderm bacteria (a component of the so-called Tol-Pal system) (*7*, *8*). In these channels, the proton flow is thought to generate cyclical interactions between the motor and a cognate outer-membrane (OM) complex via retractile periplasmic domains (*9*, *10*). In *Escherichia coli*, TolQR localizes to the division septum, and its activity allows the spatial recruitment of the Pal OM protein for the completion of cytokinesis (*11*). Similarly, AglRQS activity is thought to interact with the Glt, an 11-protein complex (GltA to GltK), connecting with the surface and promoting the exposure of an associated adhesin, CglB (*12*) at bFAs (Fig. 1A).

2) Active motility complexes are formed at the cell pole where the Agl-Glt system is recruited to a so-called cytoplasmic platform formed by a number of cytoplasmic proteins. At least three of these proteins have been identified: the actin-like protein MreB, the coiled-coil protein AglZ (Fig. 1B), and the Ras-like small guanosine triphosphatase (GTPase) protein Mutual gliding-motility protein (MglA). Within this platform, AglZ and MglA interact (*13*); each of these proteins could also interact with MreB (*14*, *15*). In particular, MglA only binds MreB in its active guanosine 5′-triphosphate (GTP)–bound form (*15*). Beyond these interactions, the exact architecture of the cytosolic platform is not known. Both AglZ and MglA localize to bFAs (*15*, *16*), but the physical connection between the cytosolic platform and the Agl-Glt complex has not been determined.

3) The molecular basis of the helical directionality of the Agl-Glt complex (*4*) is not understood. It has been proposed to emerge from polarized interactions with the bacteria peptidoglycan, perhaps guided by MreB itself (*17*), analogous to its function in guiding peptidoglycan

[1]Laboratoire d'Ingénierie des Systèmes Macromoléculaires (LISM), Institut de Microbiologie de la Méditerranée (IMM), CNRS - Aix-Marseille Université UMR7255, 31 Chemin Joseph Aiguier CS70071, 13402 Marseille Cedex 20, France. [2]Laboratoire de Chimie Bactérienne (LCB), Institut de Microbiologie de la Méditerranée (IMM), Turing Center for Living Systems, CNRS - Aix-Marseille Université UMR7283, 31 Chemin Joseph Aiguier CS70071, 13402 Marseille Cedex 20, France. [3]Institut de Microbiologie de la Méditerranée (IMM), CNRS - Aix-Marseille Université UMR7283, 31 Chemin Joseph Aiguier CS70071, 13402 Marseille Cedex 20, France. [4]National Center for Biotechnology Information, National Library of Medicine, National Institutes of Health, Bethesda, MD 20894, USA. [5]Department of Microbiology and Molecular Medicine, Faculty of Medicine/Centre Médical Universitaire, University of Geneva, 1211 Genève 4, Switzerland.
*Corresponding author. Email: elantak@imm.cnrs.fr (L.E.); tmignot@imm.cnrs.fr (T.M.)
†These authors contributed equally to this work.

synthetic machineries; however, this is not currently supported by experimental evidence. Nevertheless, several lines of evidence suggest that MglA-GTP regulates both bFA activity and directionality via its GTP cycle. In support of this, GTP-locked MglA variants (MglA$^{Q82A/L}$) produce hyperstable bFAs with directionality defects (*15*, *18*). In vivo, the MglA GTPase activating protein (GAP), MglB, interacts directly with MglA and activates GTP hydrolysis (*16*, *19*). MglB mostly localizes at the lagging cell pole, which ensures the disassembly of the motility complex at that pole (*16*, *19*). Despite this localization, there is evidence that MglB establishes an MglA-GTP gradient that affects bFAs activity along the cell axis (*18*). Not only this effect could be mediated at a distance, but it could also be due to a direct action of MglB at bFAs.

How MglA and other platform proteins connect to the Agl-Glt system is not understood, and, thus, a molecular mechanism for the dynamic assembly and disassembly is lacking. On the basis of two-hybrid analyses and cross-linking experiments, an interaction between MglA and a protein from the molecular motor, AglR, has been proposed, but how it connects to the functional assembly of bFAs is not known (*18*). In this study, we find that the connection occurs mainly via direct interactions between the GltJ protein and the platform proteins MglA and AglZ. These interactions not only drive bFA assembly but also regulate their turnover via an embedded molecular switch, allowing MglB to inactivate MglA near the lagging cell pole.

RESULTS

GltJ is a bFA protein

To identify how the cytosolic platform connects to the Agl-Glt machinery, we focused on Glt proteins predicted to localize to the IM and contain extended cytosolic (effector) domains (*5*, *6*). Among them, GltJ (also known as AgmX) (*6*) harbors a predicted cytosolic region linked to a single transmembrane helix and exposes a flexible poorly structured region, followed by a TonB-C domain in the periplasm (Fig. 2A), which is related to the C-terminal domain of the TonB proteins (*4*, *5*, *20*). GltJ could participate in energy transduction and interact with the Agl motor (*4*). Consistent with this, a *gltJ*

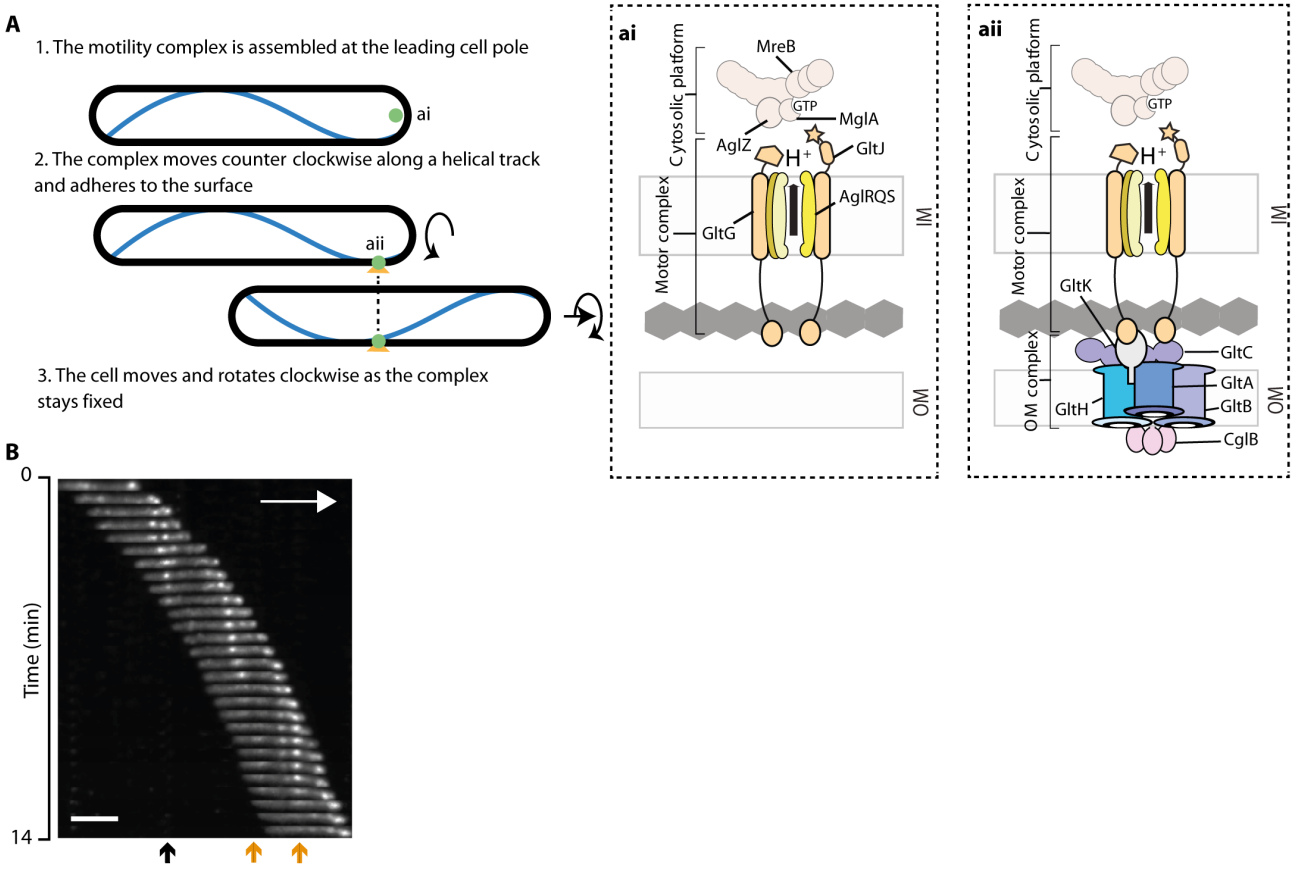

Fig. 1. Dynamics of the *M. xanthus* motility complex. (**A**) Proposed architecture of the motility complex and mechanism of propulsion. (ai) Proposed structure of the trafficking motor complex in nonadhered mobile clusters. The motility complex is assembled at the leading cell pole by recruitment of the IM motors (GltJ, GltG, and AglRQS) to the cytosolic platform formed by the AglZ, MglA, and MreB proteins. This complex uses the proton-motive force to move directionally to the lagging cell pole in a counterclockwise rotational trajectory, until it becomes immobilized at bFA. (aii) Interaction between the IM motor and a complex of OM proteins containing the CglB adhesin is proposed to connect the trafficking complex to the underlying substratum and form bFAs. The motility complex becomes fixed as OM adhesive complex treadmill through the IM motor via proton-motive force (pmf)-driven interaction cycles. The cell moves, rotating along its long axis in the clockwise direction. (**B**) *Myxococcus* bFAs containing AglZ-NG imaged by epifluorescence. Fixed clusters are formed at the leading cell pole and either disperse when they reach the lagging cell pole (black arrow) or disperse along the cell body (orange arrows). White arrow indicates the direction of movement. Pictures were taken every 30 s. Scale bar, 2 μm.

mutant is defective in bFA-dependent motility (Fig. 2, B and C) (*5*, *6*). To demonstrate that GltJ is a structural component of the Agl-Glt complex, we first constructed a stable N-terminal NeonGreen (NG)–GltJ protein (fig. S1A) and analyzed its localization in cells. Single cells expressing NG-GltJ were motile, only showing a slight reduction in speeds (Fig. 2C), indicating that NG-GltJ is mostly functional. Although the localization of NG-GltJ was more dispersed than AglZ-NG (Fig. 1B), it also assembled at the leading cell pole and formed bFAs, which was most evident in a kymograph representation (Fig. 2D and movie S1). We conclude that GltJ is a component of the Agl-Glt complex when it is recruited at bFAs.

A cytosolic region of the GltJ protein is required for the formation of bFAs

GltJ has an extended 377 residues N-terminal region predicted to localize to the cytosol (Fig. 2A). More specifically, the first 222 residues (Nt1-222) contain a predicted zinc-finger (ZnR) domain (residues 1 to 42; fig. S2A) connected to a predicted Glycine-Tyrosine-Phenylalanine (GYF) domain (residues 138 to 222; fig. S2B) via a flexible Linker region of 95 residues. GYF domains are involved in protein-protein interactions (*21*), and they are present in most major bacterial lineages, with a notable overrepresentation in Deltaproteobacteria, Gammaproteobacteria, Bacteroidetes, Planctomycetes-Verrucomicrobia, Firmicutes, and Actinobacteria (fig. S3). Like in GltJ, most of these bacterial GYF proteins have a characteristic domain architecture characterized by a GYF domain at the N terminus (a statistically significant bias for N-terminal location: χ^2, $P = 7.1 \times 10^{-4}$), followed by a C-terminal membrane–associated receptor module (fig. S4).

ZnR domains are ligand-binding domains involved in nucleic acids–protein or protein-protein interactions (*22*) (see below). Approximately 44% of all bacterial proteins containing a GYF domain combine it with an adjacent ZnR domain (figs. S3 and S4), which occurs either N terminus to the GYF (primarily in myxobacteria and planctomycetes) or its C terminus in several members of the polyvinyl chloride clade of bacteria (figs. S3 and S4). The co-occurrence of these domains in bacteria suggests a conserved complementary mode of action.

Since Nt1-222 might contain important ligand binding motifs in the cytosol, we expressed a GltJ protein lacking this region ($GltJ^{\Delta Nt1\text{-}222}$) and assayed its impact on motility. A complete motility defect was observed, similar to defects observed in *gltJ* and *aglQ* mutant strains (Fig. 2, B and C, and movies S2 and S3). We could not test the stable expression of $GltJ^{\Delta Nt1\text{-}222}$ because our antibody was raised against this region (fig. S5A). Nevertheless, expression of an NG-$GltJ^{\Delta Nt1\text{-}222}$ was stable (fig. S1) and led to the same phenotype, demonstrating the importance of the GltJ N-terminal region. We next monitored the dynamics of an NG-$GltJ^{\Delta Nt1\text{-}222}$ fusion. Contrarily to NG-GltJ, NG-$GltJ^{\Delta Nt1\text{-}222}$ was mostly diffuse, localizing to the cell pole very weakly and assembling infrequent clusters along the cell body (Fig. 2, E and F). These clusters were immobile, showing that they likely reflect defective motility complexes (fig. S5B).

To test whether Nt1-222 contains the GltJ polar targeting motif, we fused the Nt1-222 region to NG and expressed it ectopically in a *gltJ* deletion background (to avoid any interferences linked to competition of oligomerization effects; see Materials and Methods). This construct alone was sufficient to localize to the cell pole (Fig. 2G; 90.2% of $n = 631$ cells). Thus, the GltJ Nt1-222 region is essential for functional bFA assembly and contains a GltJ polar–targeting motif.

The GltJ GYF domain interacts directly with the AglZ proline-rich sequence

Since the GltJ Nt1-222 region has a polar-binding site(s), we tested whether it interacts with AglZ. AglZ is a 153-kDa protein containing an N-terminal receiver domain, followed by a proline-rich sequence (PRS) and a long coiled-coil region (Fig. 3A) (*13*). GYF domains have been previously described as adaptor domains interacting with PRS through a conserved consensus signature (*23*). However, in the GltJ GYF domain (GYF^{GltJ}), as in nearly all other bacterial GYF domains, the G, Y, and F residues (after which the domain is named) are missing (fig. S2B) (*24*). We thus tested whether GYF^{GltJ} interacts with the AglZ PRS sequence (residues 123 to 213; PRS^{AglZ}) using isothermal titration calorimetry (ITC) experiments. Complex formation was observed with micromolar affinity (Fig. 3B and table S1). The same experiment performed using the entire Nt1-222 displayed similar binding parameters, demonstrating that GYF^{GltJ} is sufficient for binding to PRS^{AglZ} (fig. S6A and table S1).

We solved the three-dimensional (3D) structure of GYF^{GltJ} by nuclear magnetic resonance (NMR) spectroscopy, which revealed a canonical GYF fold consisting of a four stranded β sheet and two α helices (Fig. 3C, fig. S6B, and table S2). This structure is conserved within the Nt1-222 as shown by the overlay of NMR fingerprint spectra where GYF^{GltJ} resonances are not perturbed in the context of the Nt1-222 region (fig. S6C). In the presence of PRS^{AglZ}, chemical shift perturbations (CSPs) were observed confirming complex formation (Fig. 3D), mostly showing resonance changes in residues from the GYF β sheet (Fig. 3, C and D, and fig. S6D). This interacting surface is clearly distinct from what has been described for canonical GYFs (fig. S6E) (*23*) and exhibits the most conserved residues among prokaryotic GYF domains (fig. S2B). GYF^{GltJ} is not able to bind a known GYF ligand sequence, the eukaryotic CD2 tail peptide (fig. S6F) (*25*), demonstrating that GYF^{GltJ} uses a new specific binding mode to recruit PRS^{AglZ}.

The interaction between AglZ and GltJ is important for bFA function

We tested the importance of GltJ and its structural motifs for the formation of bFAs containing AglZ-NG. Introduction of AglZ-NG in a *gltJ* deletion strain led to complete loss of bFA formation (Fig. 3E) (*5*, *6*). bFA formation is linked to the Nt1-222 region because bFAs also did not form in a $GltJ^{\Delta Nt1\text{-}222}$ -expressing strain (Fig. 3, E and F). Thus, AglZ recruitment is dependent on the Nt1-222 region of GltJ and should involve its interaction with GYF^{GltJ}.

We next constructed a strain expressing a GltJ protein lacking GYF^{GltJ} (*gyf*) (fig. S5A). This strain showed a significant reduction in motility speeds and mean square displacement (MSD), as compared to the wild-type (WT) (Fig. 2, B and C, and movie S4). Further introduction of AglZ-NG in the *gyf* strain revealed that bFA assembly is defective but not entirely abolished (Fig. 3E). Thus, GYF^{GltJ} is required for optimal recruitment of AglZ at bFAs for their optimal assembly. However, since abolition of the Nt1-222 region leads to loss of bFAs, AglZ must still be recruited to bFAs via another motif. As we will see below, this is likely due to the previously demonstrated interaction between AglZ and MglA (*13*).

To conversely test whether PRS^{AglZ} is required for the targeting of AglZ to bFAs, we constructed a strain expressing an AglZ protein lacking the PRS motif ($aglZ^{\Delta PRS}$). In this strain, A-motility was not

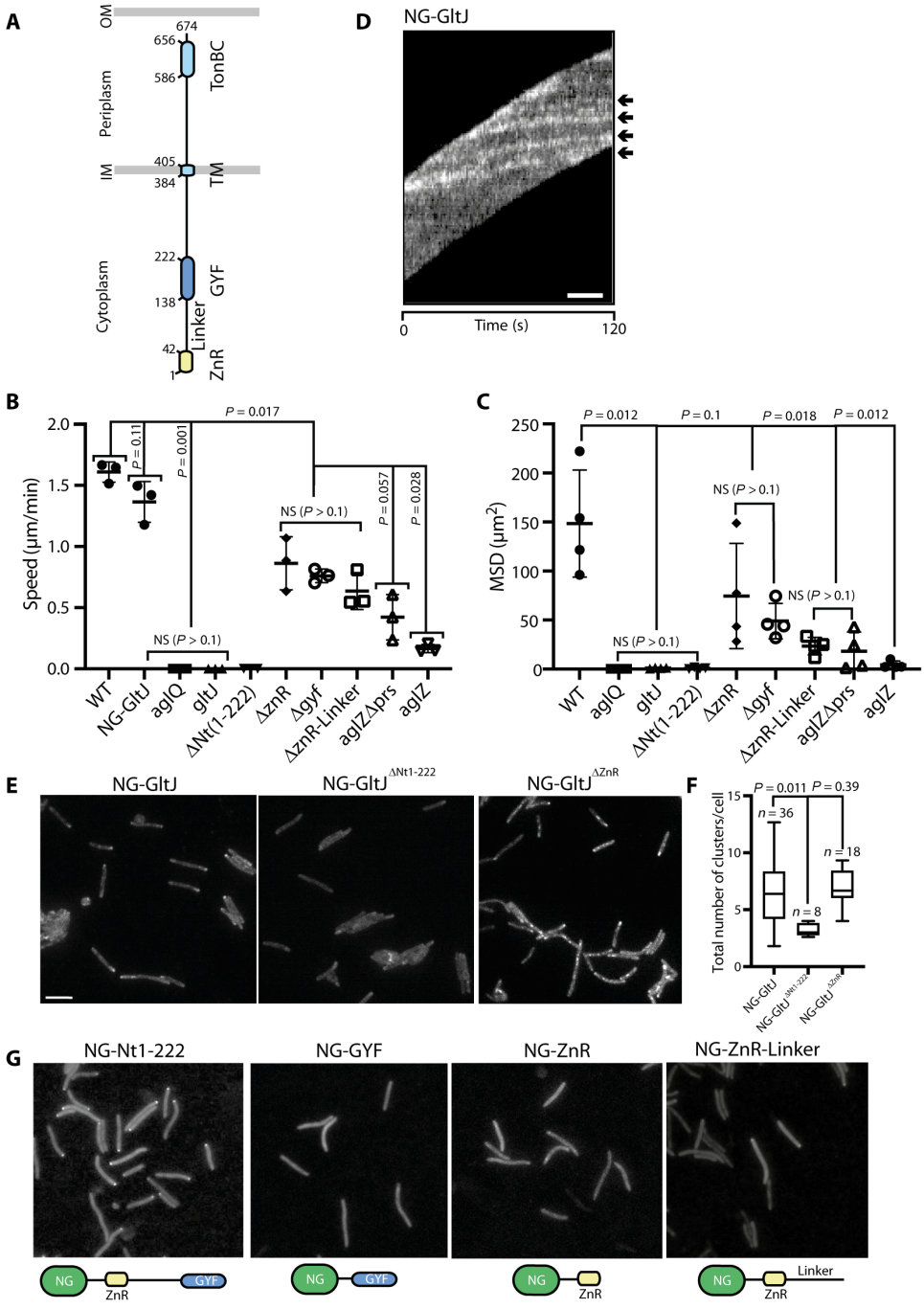

Fig. 2. The GltJ protein is essential for bFA formation. (**A**) Domain organization of GltJ and predicted topology in the cell envelope. (**B**) Single-cell speeds of *gltJ* and *aglZ* mutant strains. Each data point corresponds to the mean of the speeds obtained for single cells across four technical replicates, an experiment repeated three times for each strain. The statistics were obtained applying a Welch's *t* test. Significance is assumed for $P < 0.1$. NS, not significant. (**C**) Mean square displacement (MSD) of single cells of *gltJ* and *aglZ* mutant strains. The MSD was calculated as a proxy for directed single cell movements across a time period of 30 min (see Materials and Methods). Each data point corresponds to the mean of the MSD obtained for single cells across four technical replicates, an experiment repeated four times for each strain. The statistics were obtained as in (B). (**D**) Localization of NG-GltJ in a motile cell. Shown is a time-lapse (one image every 4 s) and derived kymograph of the same cell (one image every 1 s). The black arrows point to fixed clusters. Scale bar, 2 µm. (**E**) GltJ polar localization and localization to bFAs. Example images of NG fusions of GltJ and mutants are shown for each fusion. Scale bar, 4 µm. (**F**) Formation of GltJ clusters in cells expressing GltJ variants. Shown is the total number of GltJ-NG clusters (polar and intracellular) per cell scored in *n* replicates across four independent experiments. The statistics were obtained applying a Wilcoxon test. Significance is assumed for $P < 0.1$. (**G**) Polar determinants in the GltJ Nt1-222 region. NG fusions to various motifs of the GltJ Nt1-222 region were expressed in a *gltJ* mutant background and tested for localization. Example images are shown for each construct. Scale bars, 3 µm.

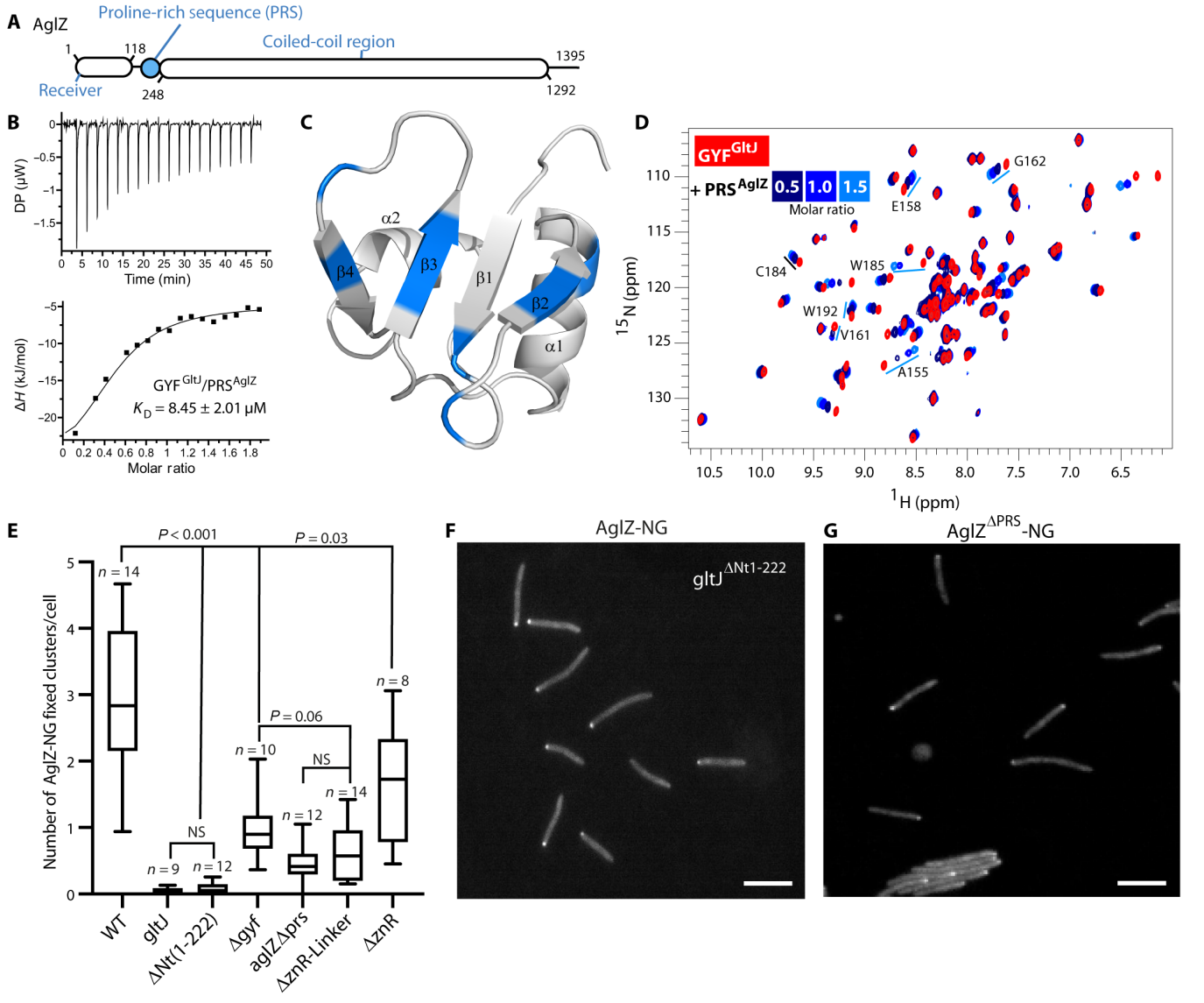

Fig. 3. GYF^{GltJ} interacts with the PRS of AglZ through a noncanonical binding interface. (**A**) Domain organization of AglZ. (**B**) ITC binding assay with GYF^{GltJ} and PRS^{AglZ}. DP, differential power. (**C**) Representative solution structure of the GYF^{GltJ} domain (NMR ensembles of the 20 conformers with the lowest energy are shown in fig. S6B). Secondary structures are labeled. The protein residues involved in the PRS^{AglZ} binding are displayed in blue. (**D**) ^{1}H,^{15}N heteronuclear single quantum coherence (HSQC) spectra, representing all H-N correlations of 0.1 mM ^{15}N-labeled GYF^{GltJ}-free (red) and upon titration of increasing concentrations of PRS^{AglZ} are shown (dark to light blue). For comparison, selected resonances of GYF^{GltJ} showing the strongest CSPs upon PRS^{AglZ} addition are reported. ppm, parts per million. (**E**) bFA activity in GltJ and AglZ mutants. For each strain, the number of active bFAs was determined by tracking individual bFAs in single cells in *n* replicates across four independent experiments. The statistics were obtained applying a Wilcoxon test. Significance is assumed for $P < 0.1$. (**F**) The GltJ N-terminal region is required for bFA formation. Scale bar, 4 μm. (**G**) The AglZ PRS motif is required for bFA formation but not for polar localization. Scale bar, 4 μm.

entirely abolished, but it was affected to a similar if not more marked extent than in the *gyf* mutant (Fig. 2, B and C, and movies S4 and S5). We could not test the stable expression of AglZ$^{\Delta PRS}$ because our raised anti-AglZ antibody could not detect AglZ from whole-cell extracts. We therefore constructed an AglZ$^{\Delta PRS}$-NG fusion that was stably expressed (fig. S7) and generated the same phenotype. In single cells, AglZ$^{\Delta PRS}$-NG is still localized to the cell pole but very rarely assembled clusters (Fig. 3, E and G).

These in vivo experiments support a physiological interaction of the GYF^{GltJ} and AglZ via PRS^{AglZ}, required for efficient bFAs assembly. However, since removing either the GYF^{GltJ} or PRS motifs does not lead to a complete loss of AglZ recruitment and motility (as seen when removing the Nt1-222 region), we hypothesized that there must be compensatory roles of the region encompassing the ZnR-Linker.

The GltJ Linker region interacts with MglA-GTP

Since the GYF domain alone is not sufficient for localization (despite its interaction with AglZ) to the cell pole, we hypothesized that MglA-GTP, which determines the localization of motility complexes at the cell pole, could also bind to the Nt1-222 region. We first tested

whether active GTP-loaded MglA interacts with individual GYF^{GltJ} and ZnR^{GltJ} domains using NMR spectroscopy. None of them showed CSPs, indicating that they do not interact (fig. S8, A and B). Then, we investigated binding of MglA-GTP to the GltJ Linker region (Linker^{GltJ}) using a ^{15}N-labeled Linker-GYF^{GltJ} construct (Fig. 4A). Linker-GYF^{GltJ} spectrum features dispersed peaks corresponding to GYF^{GltJ} resonances and also a set of peaks showing a narrow amide ^{1}H chemical shift dispersion corresponding to Linker^{GltJ} resonances, as expected for a disordered region. Eighty-five percent of all nonproline backbone amides of Linker-GYF^{GltJ} could be assigned. Upon MglA-GTP addition, GYF residue resonances were not affected, whereas several Linker resonances disappeared (residues L86 to T107), indicating interaction of MglA-GTP with a discrete motif of the Linker^{GltJ} only (Fig. 4, A and B).

Thus, two distinct GltJ regions interact with AglZ and MglA. Mixing ^{15}N-labeled Nt1-222 with both MglA-GTP and PRS^{AglZ} resulted in resonance perturbations that corresponded to individual binding of each protein to its respective ligands, the Linker motif for MglA-GTP, and the GYF domain for AglZ^{PRS} (fig. S8C).

The Linker^{GltJ} and GYF^{GltJ} exert complementary functions in vivo

We tested the function of Linker^{GltJ} in motility by constructing two additional strains: one expressing GltJ lacking the ZnR-Linker region and the other one expressing GltJ lacking the ZnR domain only (fig. S5A). Both strains were motile contrarily to the Nt1-222 strain (Fig. 2, B and C). However, in both cases, motility was affected, and

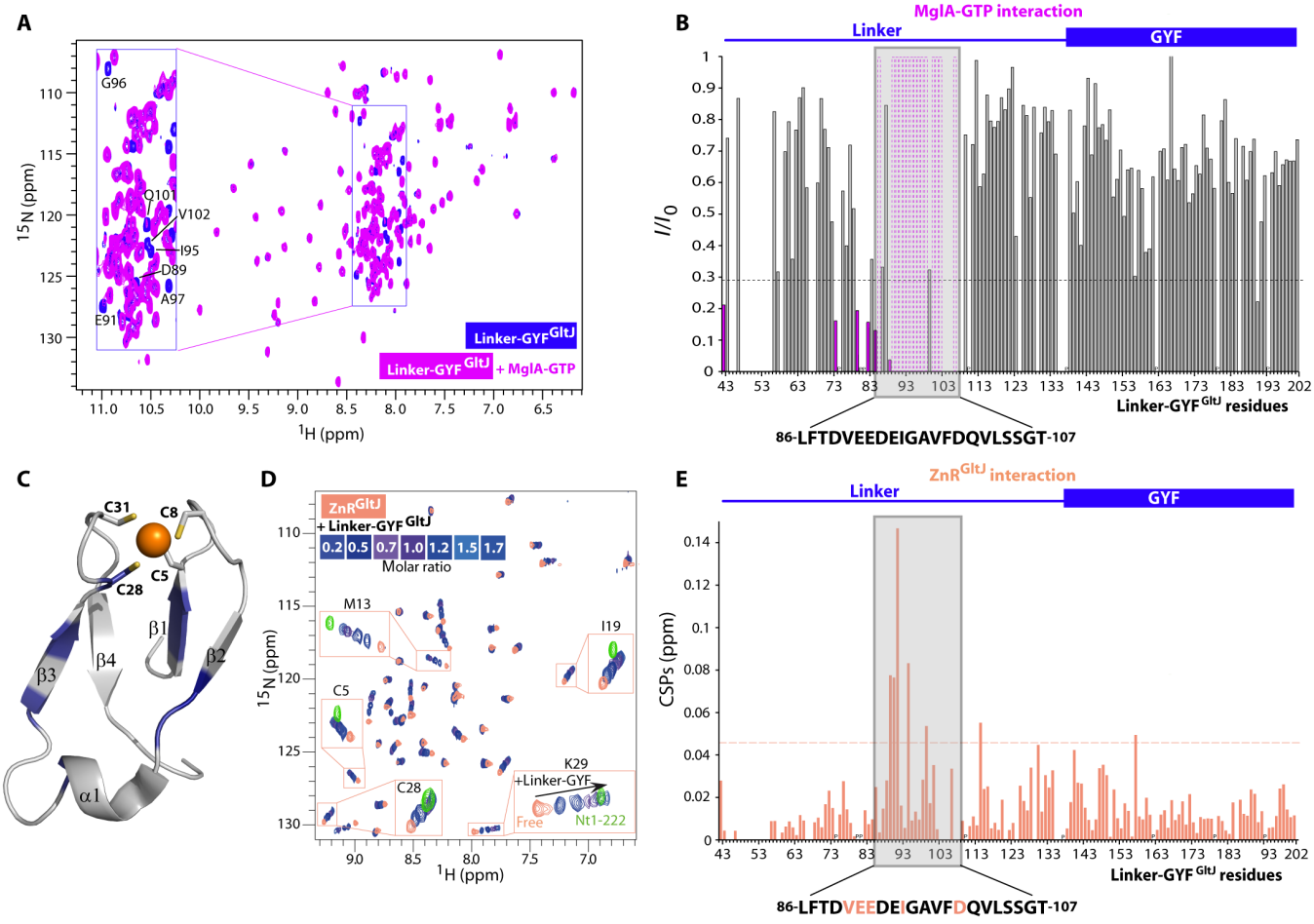

Fig. 4. MglA and ZnR^{GltJ} interact with Linker^{GltJ}. (**A**) Overlay of the ^{1}H,^{15}N HSQCs of ^{15}N-labeled Linker-GYF^{GltJ} free (blue) and bound to MglA-GTP (magenta). Left: Inset shows expanded central part of Linker-GYF^{GltJ} spectra. Peaks disappearing upon MglA-GTP interaction are labeled. (**B**) Relative peak intensities (I/I_0) of NMR signals of Linker-GYF^{GltJ} in complex with MglA-GTP. Resonances experiencing strong peak intensity decrease are indicated by magenta bars. Bars with magenta dashed edges indicate disappearing resonances upon interaction. The absence of bars indicates residues that could not be assigned, and P letters specify proline position. Dashed line represents 1σ from the average I/I_0. The main perturbed region is framed in gray, and the corresponding sequence is shown below the plot. (**C**) Representative solution structure of the ZnR^{GltJ} domain. Secondary structures are labeled as well as the cysteine side chains chelating the zinc ion (orange sphere). The protein residues involved in Linker^{GltJ} binding are displayed in blue. (**D**) ^{1}H,^{15}N-HSQC series of ^{15}N-labeled ZnR^{GltJ}-free (salmon) and upon addition of an increasing amount of Linker-GYF^{GltJ} (blue shades). Insets show selected resonances experiencing strong chemical shift variations in the presence of the Linker-GYF^{GltJ} with, in addition, the corresponding resonance in the ^{1}H,^{15}N HSQC of the Nt1-222 construct (green peaks). Residues experiencing CSPs are reported on ZnR^{GltJ} structure [shown in (C)]. (**E**) Combined CSPs between ^{1}H,^{15}N resonances of the free and ZnR^{GltJ}-bound state of Linker-GYF^{GltJ} (at 1.7 molar ratio). The absence of bars indicates residues that could not be assigned, and P letters specify the position of a proline. Dashed line represents 1σ from the average CSPs. The main region perturbed upon MglA-GTP interaction with Linker-GYF^{GltJ} is framed in gray as in (B). Residues within this region experiencing CSPs upon ZnR$_{GltJ}$ binding are colored salmon in the sequence.

while both the *znR* and *znR-linker* strains moved at reduced speeds, similar to the *gyf* strain (Fig. 2C), the *znR-linker* strain had a strongly affected MSD, suggesting an additional defect in directionality (Fig. 2C and movie S7). The defects in these two strains are indeed distinct because when we introduced AglZ-NG in each background, an intermediate effect was observed in the *znR* strain (Fig. 3E, further explored below) but the defect was pronounced in the *znR-linker* strain (Fig. 3E).

These results suggest that MglA-GTP and AglZ bind respectively to Linker^{GltJ} and GYF^{GltJ}, each acting in complementarity to bFA assembly and function. This was further evidenced when we tested the contribution of each motif to polar localization by expressing fusions of each of the ZnR^{GltJ} (NG-ZnR), the GYF^{GltJ} (NG-GYF), and the ZnR-Linker^{GltJ} (NG-ZnR-Linker) domains. The NG-ZnR and NG-GYF domains alone could not localize to the cell pole (Fig. 2G; 1.2% of $n = 1091$ and 0.6% of $n = 818$, respectively, for the ZnR and GYF). Polar localization was, however, observed for the ZnR-Linker, albeit with a lower efficiency and in a lower percentage of the cells as compared to NG–Nt1-222 (Fig. 2G; 24.2% of $n = 855$).

In summary, these results demonstrate that (i) GltJ connects the Agl-Glt machinery to the cytoplasmic platform proteins AglZ and MglA by engaging its GYF and Linker regions, respectively; and (ii) these interactions promote functional bFAs assembly. The exact interaction network between the Linker-GYF^{GltJ} motifs, on one side, and MglA-GTP and AglZ on the other side must be complex because MglA has been shown to also interact with AglZ via a region that includes a part of the PRS^{AglZ} (*13*). This could explain both why AglZ is still recruited to bFAs in *gyf* strain and why bFAs are still assembled when the Linker motif is deleted because MglA-GTP is absolutely required for bFA formation (*14*, *15*).

The ZnR domain also interacts with the Linker region

Having defined the molecular connection between the motility machinery and the cytoplasmic platform, we investigated the potential function of the ZnR domain. First, we solved the solution structure of ZnR^{GltJ} (Fig. 4C, fig. S9A, and table S2). This domain displays two double-stranded antiparallel β sheets; one strand is less compared to classical zinc ribbon domains (*26*). The structure describes two β hairpins allowing zinc chelation by the conserved cysteine residues (C5, C8, C28, and C31). The ZnR^{GltJ} structure is similar to the structure of the ZnR domain of the Zinc-finger pilus regulatory protein (ZitP), in *Caulobacter crescentus* (*22*). ZitP interacts directly with the polar organizing protein (PopZ) (*22*), which is not present in *Myxococcus*, and, thus, ZnR^{GltJ} must have a distinct ligand (see below).

Next, to assess how the ZnR^{GltJ} folds in the context of Nt1-222, we compared the NMR spectra of both constructs (fig. S9B). Unexpectedly, most of the isolated ZnR^{GltJ} resonances do not overlap with those of Nt1-222 (fig. S9B), strongly suggesting intramolecular interaction(s) between ZnR^{GltJ} and Linker^{GltJ} and/or GYF^{GltJ}. No CSPs of the ZnR^{GltJ} resonances were observed in the presence of GYF^{GltJ} (fig. S9C), discarding a direct interaction between these domains. However, perturbation was apparent when ZnR^{GltJ} was mixed with Linker-GYF^{GltJ}. The perturbed residues belong mainly to ZnR strands β1-β2-β3 (Fig. 4, C and D, and fig. S9D). The observed shifts overlapped with the resonance positions corresponding to the ZnR domain in the Nt1-222 construct (Fig. 4D, insets), confirming that the observed interaction is also present within the Nt1-222.

To determine which Linker-GYF^{GltJ} residues might interact with ZnR^{GltJ}, we performed the reverse experiment, testing NMR CSPs on ^{15}N-labeled Linker-GYF^{GltJ} in the presence of unlabeled ZnR^{GltJ} (fig. S9E). The observed perturbations concerned mainly the central part of the Linker (residues V90 to D100; Fig. 4E), a region involving residues shown to interact with MglA (Fig. 4B). Last, an 18–amino acid synthetic peptide corresponding to the Linker L86 to L103 residues led alone to chemical shift deviations of ZnR^{GltJ} resonances identical to those highlighted upon Linker-GYF^{GltJ} interaction (fig. S9, D and F), showing that this Linker^{GltJ} sequence is sufficient for binding to ZnR^{GltJ}.

Therefore, ZnR^{GltJ} and MglA-GTP share the same binding motif on the Linker^{GltJ}, suggesting that they compete for interaction with the Linker^{GltJ}. The Linker-GYF^{GltJ} resonances shifted with ZnR^{GltJ} (Fig. 4D), whereas they disappeared in the presence of MglA-GTP (Fig. 4B). This indicates a fast exchange regime between Linker-GYF^{GltJ} and ZnR^{GltJ} in contrast to a slow exchange regime between Linker-GYF^{GltJ} and MglA-GTP.

MglA-GTP competes with ZnR^{GltJ} for interaction with Linker^{GltJ}

To show that ZnR^{GltJ} and MglA-GTP can effectively compete for the same Linker^{GltJ} motif, we substituted the Linker region encompassing residue D89 to V98 by a poly-GS (glycine-serine) sequence within the Nt1-222. The NMR spectrum of the mutated Nt1-222 region (Nt1-222$^{GS89–98}$) showed that the ZnR^{GltJ} resonances were shifted to the free conformation, indicating no interaction with the modified Linker^{GltJ} (Fig. 5A). MglA-GTP interaction was also completely abolished with Nt1-222$^{GS89–98}$, confirming that MglA-GTP binds the same motif as ZnR^{GltJ} (Fig. 5B).

To further analyze the MglA-GTP binding in the full Nt-122 context, we titrated Nt1-222 with MglA-GTP (Nt1-222 for which 87% of nonproline backbone resonances were unambiguously assigned). MglA-GTP also perturbed the L86-T107 resonances (Fig. 5C). Chemical shift deviations were also observed in residues belonging to the ZnR^{GltJ} domain (Fig. 5, D and E) with several ZnR^{GltJ} residue resonances now mapping to the positions that they adopt in the ZnR^{GltJ}-free form (Fig. 5D). These results suggest that MglA-GTP binding to the Linker^{GltJ} competes with ZnR^{GltJ}, releasing its intramolecular interaction with the Linker motif and thus adopting a free conformation. Moreover, MglA binding is GTP dependent and does not occur with MglA–guanosine diphosphate (GDP) (fig. S10A).

To further support a conformational transition of ZnR^{GltJ} upon MglA-GTP interaction, we probed its metal-binding site accessibility by performing zinc/cadmium exchange experiments using NMR spectroscopy. Since cadmium presents chemical properties most similar to zinc, it can readily substitute for it, which can be monitored by changes in the NMR signals of the residues in close proximity to the metal-binding site (*27*). The exchange of coordinated Zn^{2+} for Cd^{2+} was monitored by recording a series of ^{1}H,^{15}N heteronuclear single quantum coherence (HSQC) spectra after the addition of an excess of Cd^{2+}-EDTA to ZnR^{GltJ} and to Nt1-222 in the presence or absence of MglA-GTP. As expected, the signals corresponding to amide groups in close proximity to the metal-binding site disappeared (Zn^{2+}-bound cross-peaks) and reappeared at new positions (Cd^{2+}-bound cross-peaks) over time, indicating that exchange is occurring (fig. S10, B and C). Monitoring the NMR signals of the zinc-coordinating cysteines C8 and C31 revealed faster peak disappearance when the experiment was performed with ZnR^{GltJ} (Fig. 5F and fig. S10D) in comparison to Nt1-222 (Fig. 5G and fig. S10D). In Nt1-222, the ZnR/Linker interaction might reduce the accessibility of the

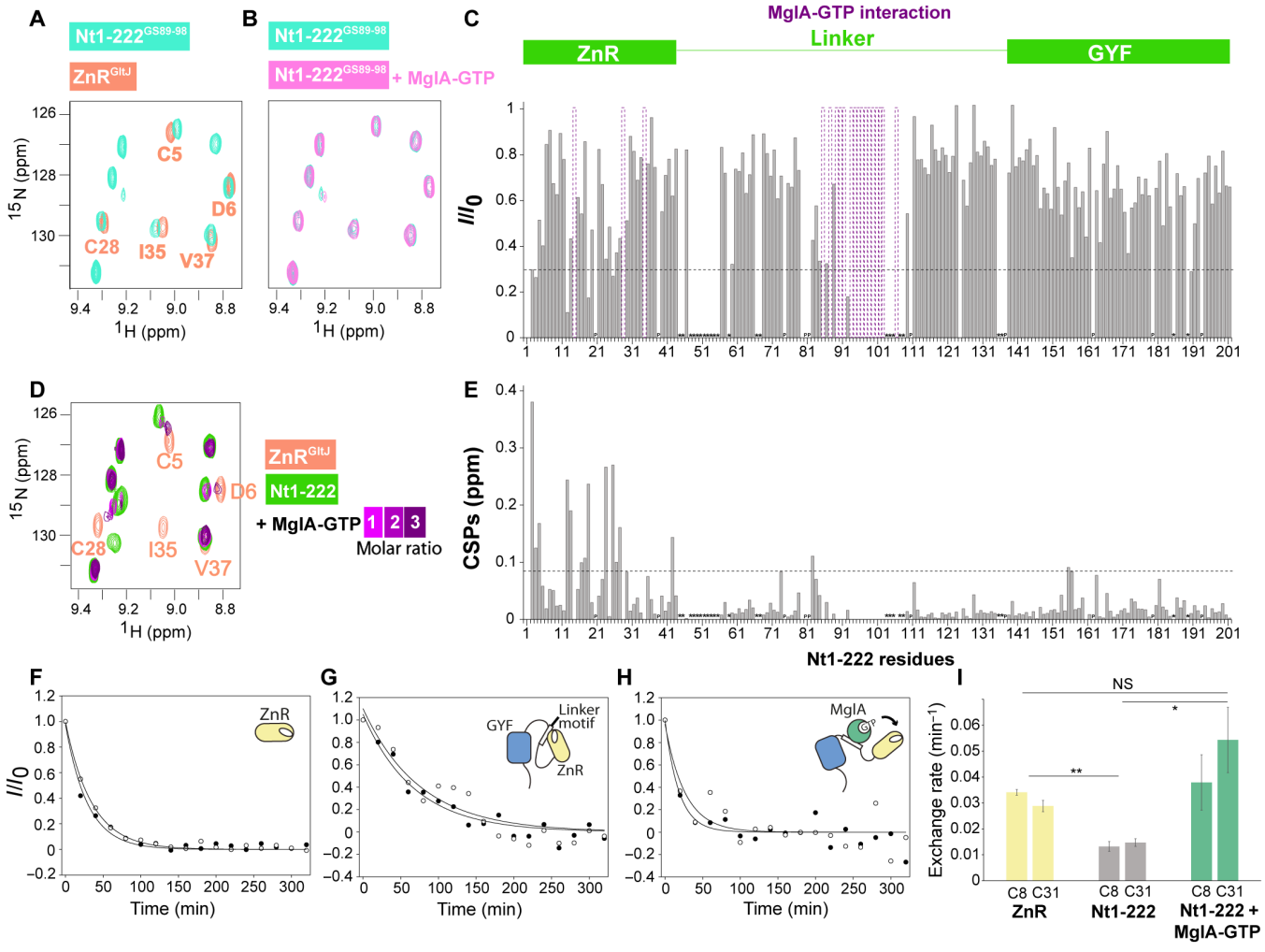

Fig. 5. MglA-GTP competes with ZnR^{GltJ} for Linker^{GltJ} binding. (**A**) Spectrum region showing the overlay of ^{1}H,^{15}N HSQC spectrum of ^{15}N-labeled Nt1-222$^{GS89–98}$ (mint), a modified Nt1-222 in which the D89-V98 region has been substituted by a poly-GS sequence, with the spectrum of free ZnR^{GltJ} (salmon). (**B**) Same spectrum region as in (A) showing the overlay of ^{1}H,^{15}N HSQC spectra of Nt1-222$^{GS89–98}$ in absence (mint) and in presence of MglA-GTP (pink). (**C**) Normalized peak intensity ratio (I/I_0) analysis of Nt1-222/MglA-GTP interaction. Bars with purple dashed edges indicate peaks disappearing upon MglA-GTP interaction. Above the plot is shown the ZnR and GYF domain limits within Nt1-222. (**D**) Spectrum region of the ^{1}H,^{15}N HSQCs of ^{15}N-labeled Nt1-222 free (green) and after addition of 1 (magenta), 2 (light purple), and 3 (purple) molar ratios of MglA-GTP. ^{1}H,^{15}N HSQC of free ZnR^{GltJ} (salmon) is also superimposed. Resonances shown correspond to ZnR^{GltJ} [same resonances shown in (A) and (B)]. (**E**) Combined CSPs of Nt1-222 bound to MglA-GTP. (**F** to **H**) Disappearance over time of ^{1}H,^{15}N HSQC cross-peaks from cysteines C8 (open circles) and C31 (filled circles) of Zn^{2+}-ZnR^{GltJ} (F), Zn^{2+}–Nt1-222 (G), and Zn^{2+}–Nt1-222 in the presence of MglA-GTP (H) upon incubation with Cd^{2+}. (**I**) Metal exchange rates derived from the experiments shown in (F), (G), and (H). The statistics were obtained applying a Student's *t* test. Significance is assumed for $P < 0.05$.

metal-binding site. In the presence of MglA-GTP, a faster C8 and C31 cross-peak disappearance is observed (Fig. 5H), indicating that interaction with MglA makes the zinc-binding site more accessible. In the presence of MglA-GTP, the Zn^{2+}/Cd^{2+} exchange rate is similar to the rate measured with ZnR^{GltJ} alone (Fig. 5I).

Together, these results demonstrate that MglA-GTP competes with ZnR^{GltJ} for the same binding site on the Linker resulting in the release of the ZnR^{GltJ} domain. Thus, depending on its binding state, the GltJ cytoplasmic region can switch between two conformations, one presumably corresponding to an ON (ZnR-free and -accessible) state and another to an OFF (ZnR-Linker–bound and –inaccessible) state. This could define an intraprotein molecular switch activated by MglA-GTP.

The ZnR domain regulates bFA function and stability in vivo

As mentioned above, a *znR* mutant shows a partial yet significant motility defect, but it still assembles bFAs (Figs. 2, B and C, 3E and movie S8). Analysis in single cells of the *znR* mutant revealed the presence of highly stable bFAs that could be tracked for extended periods of time (Fig. 6A and movie S9). The distribution of bFA stability was significantly higher in the *znR* mutant than in either the WT or *gyf* mutant (which was indistinguishable; Fig. 6B). The regulation exerted by the ZnR must go through MglA-GTP because it is absent in a *znR-linker* mutant missing the MglA-binding site (Fig. 6B and further addressed below).

To confirm the observation that the ZnR^{GltJ} domain regulates the stability of bFAs, we also compared the behaviors of NG-GltJ and a

stable NG-GltJ$^{\Delta ZnR}$ fusion (fig. S1). The NG-GltJ$^{\Delta ZnR}$ fusion also accumulated at bFAs (Fig. 2, E and F), and similarly to AglZ-NG–containing bFAs, NG-GltJ$^{\Delta ZnR}$-bFAs were more stable than bFAs formed by NG-GltJ (Fig. 6, C and D). Thus, contrarily to the GYF^{GltJ} and Linker^{GltJ} ligands that promote bFA assembly, the ZnR^{GltJ} domain, once released from the Linker by MglA-GTP, regulates bFA stability negatively, and disruption of this regulation leads to a reduction in motility speed.

The ZnR domain regulates bFA stability by recruiting MglB

Since the association of MglA with Linker^{GltJ} depends on GTP (fig. S10A), we tested whether ZnR^{GltJ} might affect its nucleotide state. ZnR^{GltJ} does not by itself interact with MglA, but it could act indirectly if once freed from its interaction with the Linker, it recruits MglB that, in turn, would dissociate MglA via its GAP activity. We therefore tested the binding of ZnR^{GltJ} to MglB by monitoring CSPs of ZnR^{GltJ} resonances upon MglB addition. Several resonances from the ZnR^{GltJ} β sheets experienced chemical shift deviations, indicating the formation of a complex between ZnR^{GltJ} and MglB (Fig. 7, A and B, and fig. S11A). The observed shifts are similar to those observed when ZnR^{GltJ} is bound to Linker^{GltJ} (Fig. 7A). Therefore, ZnR^{GltJ} interacts with Linker^{GltJ} and MglB using the same interface. This competitive interaction is evidenced by the fact that MglB cannot displace ZnR^{GltJ} from its interaction with Linker^{GltJ} since no CSP was observed when MglB was mixed with the Nt1-222 region (fig. S11B). Thus, MglA-GTP binding to Linker^{GltJ} is required to release ZnR^{GltJ}, thereby allowing it to recruit MglB (fig. S11C).

To understand how ZnR^{GltJ} interacts with MglB, we used AlphaFold to generate a structural model for the ZnR^{GltJ}/MglB complex. The predicted model (Fig. 7C and fig. S11D) not only shows involvement of ZnR^{GltJ} β sheets as demonstrated above (Fig. 7A) but also identifies the MglB C-terminal helix as the main ZnR^{GltJ}-interacting site. Consistent with this model, no CSP was observed when purified MglB lacking the C-terminal (Ct) helix (MglB$^{\Delta HCt}$) was mixed with ZnR^{GltJ} (fig. S11E).

MglB interacts with MglA-GTP in a 2:1 stoichiometry via two distinct interfaces, at the MglB dimer interface close to the switches 1 and 2 of the MglA protein, and via the C-terminal helix of one of the MglB monomers (Ct-helix-I) that inserts in an MglA pocket, opposite to the nucleotide-binding site (Fig. 7D) (*28*, *29*). The Ct-helix-I promotes interaction both with the GTP- and GDP-bound forms of MglA, which facilitates nucleotide exchange (in either direction) and therefore increases the rate of GTP hydrolysis (*28*). The structure of the C-terminal extension of the second MglB monomer (Ct-helix-II) could not be resolved in the MglA/MglB dimer complex structure (Fig. 7D). An AlphaFold model of the MglA/MglB dimer/ZnR^{GltJ} complex positions the ZnR domain as interacting with the Ct-helix-II and facing directly the GTP-binding site (Fig. 7E and fig. S11F).

To test whether the ZnR^{GltJ}/MglB interaction affects MglA-dependent GTP hydrolysis in vitro, we used a phosphate release assay that directly measures the release of Pi (*30*). As previously observed, GTP hydrolysis was negligible when MglA was incubated alone and this hydrolysis was activated by MglB (Fig. 7, F and G). The addition of ZnR^{GltJ} to MglA and MglB further activated GTP hydrolysis (Fig. 7F), inducing a fourfold increase in enzyme efficiency (k_{cat}/K_m) (Fig. 7G). This effect depends on the interaction between ZnR^{GltJ} and MglB because it was no longer observed in the presence of MglB$^{\Delta HCt}$ (Fig. 7, F and G). Together, the in vitro results are coherent with the in vivo results and suggest that the ZnR^{GltJ} domain activates bFA turnover via a direct interaction with the MglB Ct-helix-II to increase GAP efficiency and, thus, inactivation of MglA at bFAs.

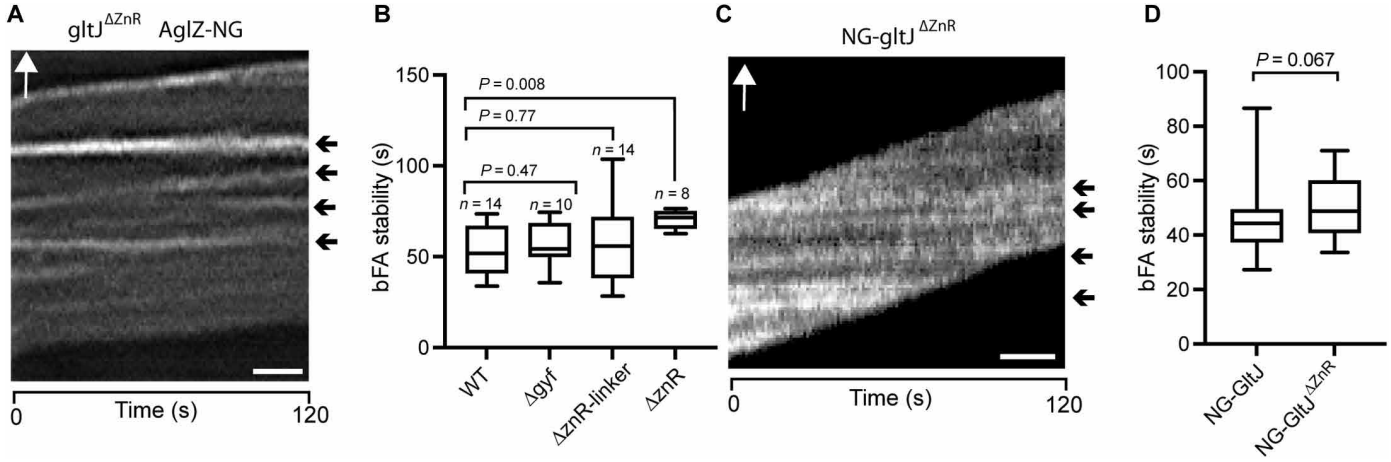

Fig. 6. The Linker^{GltJ} region and the ZnR^{GltJ} domain are functional in vivo. (**A**) AglZ-NG forms highly stable bFAs in a GltJ$^{\Delta ZnR}$-expressing strain. Shown is a kymograph of a single cell with images captured every 1 s for 120 s. Scale bar, 1 μm. (**B**) AglZ-containing bFA stability in GltJ mutant–expressing strains. For each strain, the stability of individual bFAs was tracked in single cells. For each strain, the mean cluster stability was determined for *n* replicates across four independent experiments. The statistics were obtained applying a Wilcoxon test. Significance is assumed for $P < 0.1$. (**C**) NG-GltJ$^{\Delta ZnR}$ forms highly stable clusters. Shown is a kymograph of a single cell with images captured every 1 s for 120 s. Scale bar, 1 μm. (**D**) bFA stability in NG-GltJ and NG-GltJ$^{\Delta ZnR}$ strains. For each strain, the stability of individual bFAs was tracked in single cells. For each strain, the mean cluster stability was determined for *n* replicates across four independent experiments. The statistics were obtained applying a Wilcoxon test. Significance is assumed for $P < 0.1$.

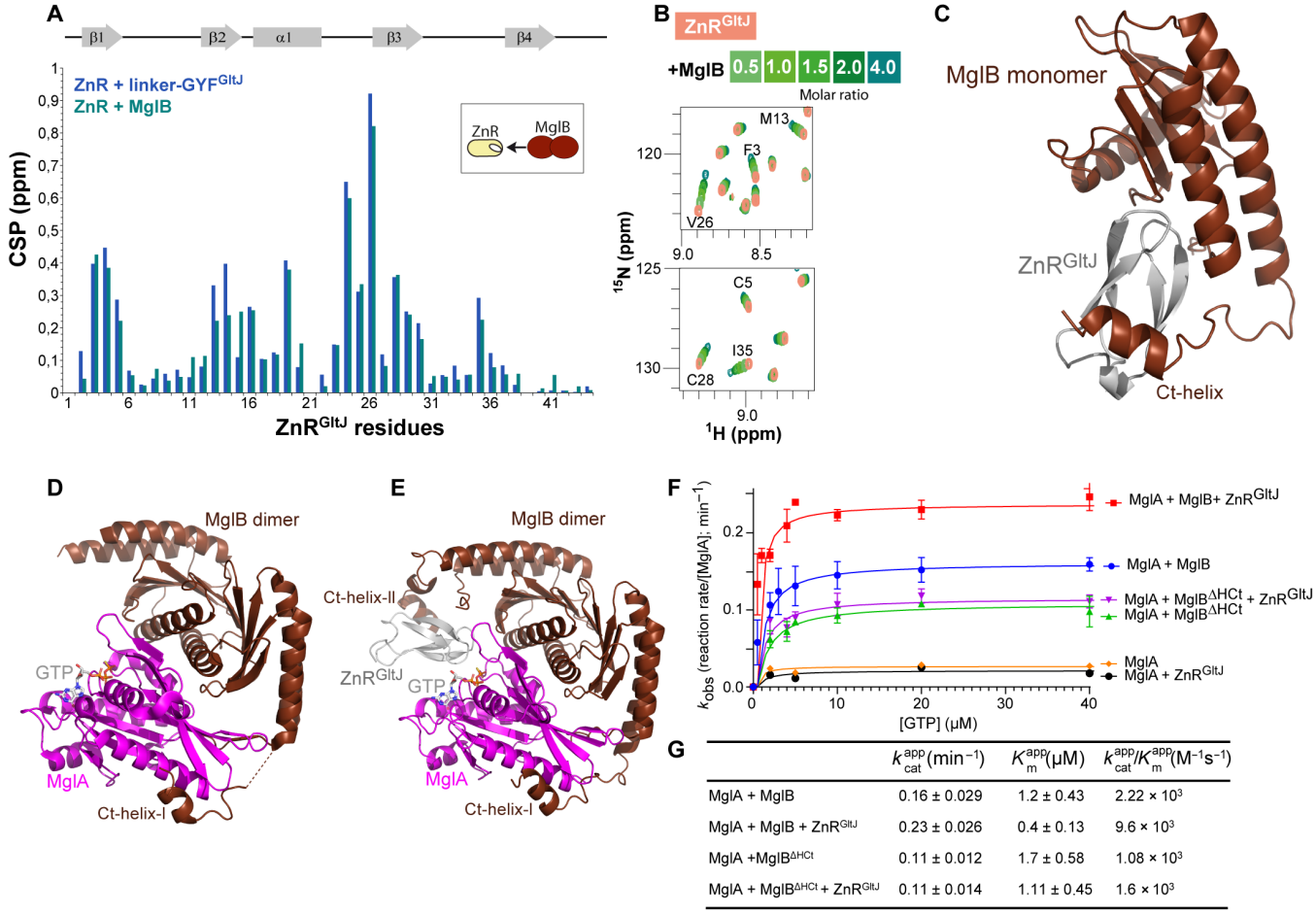

G

	k_{cat}^{app} (min^{-1})	K_m^{app} (μM)	k_{cat}^{app}/K_m^{app} (M^{-1}s^{-1})
MglA + MglB	0.16 ± 0.029	1.2 ± 0.43	2.22 × 10^3
MglA + MglB + ZnR^{GltJ}	0.23 ± 0.026	0.4 ± 0.13	9.6 × 10^3
MglA +MglB^{ΔHCt}	0.11 ± 0.012	1.7 ± 0.58	1.08 × 10^3
MglA + MglB^{ΔHCt} + ZnR^{GltJ}	0.11 ± 0.014	1.11 ± 0.45	1.6 × 10^3

Fig. 7. ZnR^{GltJ} interacts with MglB. (**A**) Combined CSPs between ^{1}H,^{15}N resonances of the free ZnR^{GltJ} and upon binding to Linker-GYF^{GltJ} (blue bars) or MglB (blue-green bars). The secondary structures of ZnR^{GltJ} are indicated above the plot. (**B**) Spectrum regions of ^{1}H,^{15}N HSQC series of ^{15}N-labeled ZnR^{GltJ} free (salmon) and upon addition of increasing amounts of MglB (green shades) up to four molar excess. (**C**) AlphaFold structure p4rediction of the MglB/ZnR^{GltJ} complex. (**D**) Crystal structure of MglA–guanosine 5′-*O*-(3′-thiotriphosphate) (GTP-γ-S) bound to MglB homodimer [Protein Data Bank (PDB) ID: 6IZW] (*28*). (**E**) AlphaFold structure prediction of the MglA/MglB dimer/ZnR^{GltJ} complex. The GTP-γ-S position was inferred by homology to the structure of MglA–GTP-γ-S/MglB dimer shown in (D). (**F**) Initial rate data for Pi release at different concentration of GTP in presence of MglA (orange), MglA + MglB (blue), MglA + MglB + ZnR^{GltJ} (red), MglA + MglB^{ΔHCt} (green), and MglA + MglB^{ΔHCt} + ZnR^{GltJ} (purple). (**G**) Kinetic parameters table. Initial rate data were fitted to the Michaelis-Menten equation. The assays were performed using constant concentration of proteins (MglA, 2 μM; MglB and MglB^{ΔHCt}, 4 μM; ZnR^{GltJ}, 8 μM) and a range of GTP concentrations (0.5 to 100 μM).

DISCUSSION

Whether in eukaryotes or bacteria, FAs have to be dynamic, and their formation and disassembly must be tightly controlled to enable cell migration. Here, linking atomic resolution to single-cell studies, we establish the GltJ protein as a critical factor for bFA assembly and dynamics in vivo. The function of GltJ elucidates the connection between the Agl/Glt complex and the bFA cytosolic platform, revealing that complementary interactions between GltJ, MglA-GTP, and AglZ activate the motility complex. We also demonstrate that GltJ exerts a regulatory function through a conformational transition, switching from an OFF to an ON state. Thus, the interaction between GltJ and the bFA cytosolic platform not only reveals how these two modules are physically connected but also explains how this connection is modulated along the cell body.

On the basis of these results, we can propose a concise molecular model that sheds light on the assembly and regulation of bFAs in gliding *M. xanthus* cells (Fig. 8). In its inactive state, the IM Agl-Glt complex is not engaged with the cytosolic platform and localizes itself around the cell periphery. During this phase (state 1), the N-terminal domain of GltJ adopts an OFF conformation, where the ZnR^{GltJ} domain interacts with the Linker^{GltJ} central motif.

The turning point toward activation occurs at the leading cell pole. Here, AglZ and MglA-GTP establish interactions with the GYF^{GltJ} and Linker^{GltJ} motifs, respectively. Although it is not clear how these two proteins cooperate at these sites, the interaction with MglA-GTP triggers a switch of the ZnR^{GltJ} domain into the ON conformation (transitioning to state 2). At the cell pole where MglA-GTP concentrations are high, this new conformational state activates the Agl-Glt complex, setting it on a movement along a helical trajectory [potentially guided by the platform-associated MreB actin-like protein (*17*)] and forming bFAs when they interact with the OM complex (reaching state 3).

As the motility complex steadily advances toward the rear of the cell, the local concentration of MglB increases (although this is yet

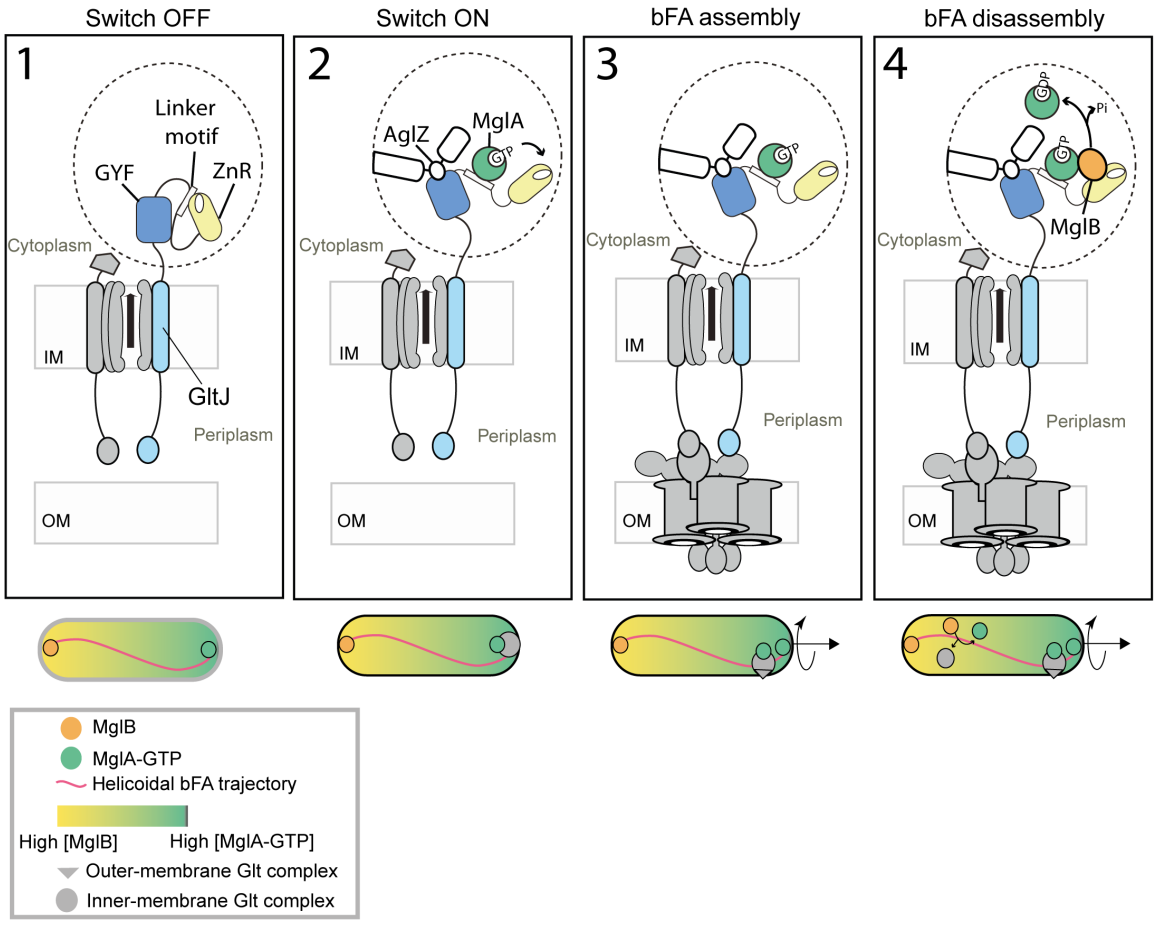

Fig. 8. Dynamic assembly of the Agl-Glt complex in motile *Myxococcus* cells. The upper cartoon depicts the proposed activation/deactivation mechanism of bFAs via connection of the Agl-Glt machinery to the cytoplasmic platform by the GltJ three motifs N-terminal region. For clarity purposes, additional interactions such as MglA/AglZ and MglA/MreB have been omitted. Although it is clear that these interactions are important for bFA assembly, how they integrate with the switch remains to be determined. The lower cartoon represents the cellular location of GltJ-containing complexes for each step of the proposed model. The MglA-MglB proposed concentration gradient within the cell is represented as an orange to green color gradient along the cell axis. 1. When the Agl-Glt complex is inactive and not connected to AglZ and MglA, the switch is OFF, and the ZnR domain is in the closed state through interaction with the Linker motif. 2. At the leading cell pole, the Agl-Glt complex becomes activated via the independent docking of the GYF^{GltJ} domain to AglZ and the Linker motif to MglA-GTP, and the ZnR switch is in the free ON conformation. The complex can thus move toward the lagging cell pole. 3. In the front of the cell where MglA concentrations are high, motility IM complexes form bFAs when they interact with the OM complex and thus adhere to the underlying substratum. 4. At the back of the cell where MglB concentration is higher possibly because of the MglA-GTP gradient, MglB is recruited by the ZnR^{GltJ} and exerts its GAP activity to convert MglA to the GDP-bound state that cannot bind the Linker motif and thus dissociates from GltJ. Ultimately, this regulation leads to the release of the cytoplasmic platform and back to step 1.

to be shown that MglB forms an opposite gradient), which locally prompts an interaction with the ZnR^{GltJ} and provokes the detachment of MglA, causing the dispersion of the Agl-Glt complex from bFAs (transitioning to state 4). The assembly of new bFAs at the cell pole ensures ongoing movement in the forward direction.

It is worth noting that the regulation of bFAs by MglB is mostly important along the cell body and not absolutely required at the lagging cell pole where the motility complexes are still disassembled in the *znR* mutant. At this pole, the elevated concentration of MglB could conceivably suffice to detach MglA from GltJ. Hence, the role of the ZnR domain, particularly its augmentation of MglB-driven GTP hydrolysis efficiency, becomes especially pertinent in regions characterized by low MglB concentrations, such as the cytosolic environment [as detailed in (*16*, *31*)]. Notably, MglB has never been observed localizing at bFAs, which may not be unexpected provided that it promotes their disassembly. The RomRX complex, an MglA guanine nucleotide exchange factor (GEF) at the leading pole, which presumably contributes to the MglA gradient, can also localize to bFAs (*31*). Thus, opposite regulations might take place, reinforcing Agl-Glt activity close to the leading cell pole (RomRX) and promoting the disassembly near the lagging cell pole (MglB). This spatial regulation could ensure that the activity of multiple bFAs assembled is spatially concerted within a cell. In support of this, *znR* mutant cells exhibit a notable reduction in movement speed, implying that propulsion is impaired when the complexes are stabilized.

In bacteria, contiguous ZnR-GYF motifs are always separated by a variable flexible Linker, suggesting that they also function as switches. However, the ligands (and thus functions) are likely variable because outside of the Myxococcales, there is no correlation between the presence of ZnR-GYF proteins and the highly mobile

MglA-MglB–type operons or an AglZ-like protein. These observations collectively suggest that dual ZnR and GYF domain proteins are prevalent across bacterial species, likely serving as versatile switch modules adept at binding a spectrum of partners beyond the confines of the Myxococcales Mgl/Agl-Glt system. Given that these proteins can interface with diverse extracellular regions or transmembrane domains and are often encoded in conserved operons alongside genes for receptor-like transmembrane proteins (fig. S4), we propose that, akin to GltJ, they facilitate signaling between the extracellular and intracellular compartments.

Last, in eukaryotes, eFAs are dynamic structures where autoinhibition mechanisms integrate intracellular and extracellular signals to promote directed cell migration. This spatial regulation of eFAs also relies on the modulation of small G proteins via the spatiotemporal recruitment of GAP and GEF activities (i.e., via the activity of focal adhesion kinase) (*32*). The GltJ-MglAB system shows that bFAs might be just as sophisticated and could adapt the motility complex to changes in the extracellular environment or to the presence of other cells. During predation, contact with prey cells induces rapid bFA disassembly that is coupled to assembly of a Tad-like machinery (Kil) at the prey contact site (*33*). The precise mechanism underlying this process remains speculative. However, the unique topology of GltJ positions it as an ideal protein candidate capable of functioning as a bidirectional sensor/receptor. GltJ not only modulates the OM Glt complex following recruitment by the cytosolic platform but also senses OM perturbations, thereby influencing its interaction with the cytosolic platform.

MATERIALS AND METHODS

Bacterial strains, plasmids, and growth

Strains, plasmids, and primers used for this study are listed in tables S3 to S5. All genetic mutants were constructed in the *M. xanthus* DZ2 strain. *M. xanthus* strains were grown at 32°C in casitone yeast extract–rich medium as previously described (*34*). The deletion strains and the strains expressing the different NG fusions were obtained by a double recombination strategy as previously described (*34*). Briefly, deletion alleles or the NG fusion alleles (under the control of their native promoters) were Gibson assembled into the suicide plasmid pBJ114 (*galK*, Kan^R) and used for allelic exchange. Plasmids were introduced in *M. xanthus* by electroporation. After galactose selection, clones were identified by polymerase chain reaction. For complementation of Δ*gltJ* strain, pSWU30 plasmid (Tet^R) was used to allow ectopic expression of the corresponding genes sequences of the individual domains of GltJ from the *gltJ* native promoter at Mx8-att site (*16*).

Western blotting

Samples were grown at 32°C in casitone yeast extract medium until they reached an optical density at 600 nm (OD_{600}) of 0.5 to 0.8. One milliliter of culture was then centrifuged for 5 min at 8000 rpm, and the pellet was resuspended in 1× SDS–polyacrylamide gel electrophoresis loading buffer with β-mercaptoethanol to 0.1 OD /10 μl. Samples were then heated for 10 min at 99°C, and 10 μl were loaded on a commercial 4 to 20% SDS–polyacrylamide gel electrophoresis (Bio-Rad). Electrophoresis was performed at 200 V for 30 min at room temperature (RT). For Western blotting, proteins were transferred onto nitrocellulose membranes (at RT for 1 hour at 100 V), blocked for 30 min at RT in 1× tris-buffered saline, 0.05% Tween 20, and 5% milk. Then, the membranes were incubated with 1:5000 dilutions of polyclonal α-NtermGltJ (raised for this study) for GltJ full or domains or with 1:500 dilutions of commercial monoclonal α-NeonGreen (ChromoTek) in blocking buffer for 2 hours at RT or ON at 4°C. After three washes for 10 min in 1× tris-buffered saline and 0.05% Tween 20, the membranes were incubated with 1:5000 goat anti-rabbit horseradish peroxidase conjugate (Bio-Rad) for GltJ and with 1:5000 goat anti-mouse horseradish peroxidase conjugate for NG in blocking buffer. Then, the peroxidase reaction was developed by chemiluminescence [SuperSignal West Pico (or Femto) chemiluminescent substrate, Thermo Fisher Scientific], scanned, and analyzed with ImageQuant LAS4000 and TL analysis software (GE Healthcare Life Sciences).

Single cell motility assays

Total internal reflection fluorescence microscopy

Cells were grown ON at 32°C until they reached an OD_{600} of 0.4 to 0.6 and then resuspended in TPM buffer (10 mM Tris-HCl, pH 7.6, 8 mM $MgSO_4$,and 1 mM KH_2PO_4) at OD_{600} of 2, and 2 μl were spotted on a TPM of 1.5% agar pads poured inside a gene frame (Thermo Fisher Scientific, Gene Frame) taped to a microscope slide. An SR cover glass (Marienfeld Superior, Precision cover glasses no. 1.5H) was then used to seal the preparation. Imaging was performed on a DeltaVision SR Imaging System (GE Healthcare) with an Olympus PlanApo N 60× 1.49 NA oil immersion objective and liquid-cooled scientific complementary metal-oxide semiconductor camera (IMM Microscopy Platform). Images were acquired using a laser excitation at 488 nm and an intensity laser at 5% during 200 ms. For each acquisition, a ring–total internal reflection fluorescence illumination was generated with an angle around 80° and 85°. The angle was chosen manually to see focal adhesion complexes as clearly as possible. NG fluorescence was then recovered between 504 and 576 nm. To generate the movie, an image of 1024 by 1024 pixels was acquired every 1 s during 2 min (stack of 121 images).

Automated cell tracking and statistics

The tracking workflow was designed as follows

Cells to be analyzed were selected manually and kymographs were generated under Fiji (*35*) to determine the displacement of the cell center and the two poles. The fluorescent foci were then annotated manually by drawing polygons delineating foci traces directly on the kymograph. A Fiji macro was then used to produce data files in .csv format that contain all the information of the cell: movement, type of cell, type of foci, number of foci, displacement of foci, etc. The obtained files were then subjected to an R script that produced a pdf report for each cell: The calculated parameters were as follows:

1) Cell movement = sum of cell displacements relative to the substrate.

2) The relative motion of each cluster = sum of the displacements of the cluster with respect to the center of the cell.

3) The MSD of the cell.

4) The MSD of the focus.

5) The periods of movement and stop of the cell

These parameters are calculated raw or normalized to the duration of the movement.

Protein expression and purification

ZnR^{GltJ} (1 to 42)– and GYF^{GltJ} (138 to 222)–isolated domains were expressed and purified as previously described (*24*). PRS^{AglZ} (123 to

213), Nt1-222 (1 to 222), Nt1-222$^{GS89–98}$, and Linker-GYF^{GltJ} (43 to 222) were produced as N-terminal His6-tagged lipoyl fusion proteins. Overexpression was induced in *E. coli* cells with 1 mM isopropyl-β-D-thiogalactopyranoside at an OD_{600} of 0.6 to 0.7, followed by 16-hour incubation at 25°C. After harvesting by centrifugation, the cell pellet was resuspended in lysis buffer [20 mM tris-HCl (pH 8), 500 mM NaCl, and 20 mM imidazole] supplemented with cOmplete EDTA-free protease inhibitor cocktail (Roche). The cell suspension was lysed using high-pressure homogenizer (Avestin Emulsiflex C5). The whole-cell extract was cleared by centrifugation at 90,000*g* for 30 min. Next, the supernatant was loaded on a HisTrap HP column (Cytiva) and eluted with an imidazole gradient. The fractions containing the target proteins were pooled and dialyzed overnight at 4°C in the presence of Tobacco Etch Virus (TEV) protease. The excess TEV protease and His-lipoyl tag were removed using a HisTrap HP column. The protein samples were further purified using a Superdex-75 column equilibrated with NMR buffer [20 mM tris-HCl (pH 7), 50 mM NaCl, 10 mM $MgCl_2$, and 1 mM dithiothreitol (DTT)]. Purified proteins were concentrated by membrane filtration. Protein concentrations were determined by absorbance at 280 nm using the theoretical extinction coefficient. MglA, MglB, and MglB$^{\Delta HCt}$ proteins were produced and purified as previously described (*29*). CD2 tail and Linker^{GltJ} (86 to 103) peptides were chemically synthesized (Schafer-N, Danemark).

Isothermal titration calorimetry

ITC was used to evaluate the thermodynamics parameters of the binding between GYF^{GltJ} or Nt1-222 and PRS^{AglZ} protein domains. Titrations were carried out on a MicroCal PEAQ-ITC (Malvern, UK) microcalorimeter at 25°C. For each experiment including controls, 19 injections have been set with the first injection set at 0.4 μl and the 18 following injections at 2 μl. Duration of each injection was 4 s, and the interval between each injection was 150 s. All experiments were performed in a 10 mM $NaPO_4$ (pH 7) ITC buffer. PRS^{AglZ} was loaded into the sample cell, and GYF^{GltJ} or Nt1-222 was loaded into the syringe. Control experiments were performed in which the ITC buffer was titrated into PRS^{AglZ} alone to account for heat released because of dilution. This background was subtracted from test data before final dissociation constant was calculated. Data were analyzed using the MicroCal PEAQ-ITC Analysis software.

Nuclear magnetic resonance

NMR spectroscopy

All NMR experiments were performed on Bruker spectrometers equipped with cryogenically cooled TCI probeheads, operating at 950 or 600 MHz. The experiments were processed using Bruker Topspin and analyzed using CcpNmr Analysis (*36*).

NMR structure determination

ZnR^{GltJ}- and GYF^{GltJ}-isolated domains have been produced as uniformly ^{13}C,^{15}N-labeled proteins. Backbone and side-chain resonance assignments have been previously performed (*24*) and are available under Biological Magnetic Resonance Bank accession numbers 51104 and 51096 for ZnR^{GltJ} and GYF^{GltJ}, respectively. The 3D protein structures were calculated with the program CYANA using Nuclear Overhauser Effect (NOE) distance restraints obtained from Nuclear Overhauser Effect SpectroscopY (NOESY)-based NMR experiments and angular restraints (phi and psi) derived from chemical shifts of backbone atoms using the TALOS+ software program (*37*). In addition, hydrogen bonds restraints were extracted from HNCO-COSY experiments (*38*) and then included for structure calculations. For ZnR^{GltJ}, distance restraints for the zinc ion coordinated to the corresponding cysteines were introduced as pseudo-NOEs (*39*). The 20 final structures from CYANA were then water refined with AmberTools22 and Amber22. ZnR^{GltJ} topology and parameter files were prepared using the ZAFF Modeling Tutorial. The best 20 structures were selected on the basis of the lowest total energy and analyzed using Procheck_NMR.

Backbone resonance assignment of the Linker-GYF and Nt1-222 constructs

Backbone ^{1}H, ^{15}N, and ^{13}C resonance assignments were carried on uniformly ^{13}C,^{15}N-labeled Linker-GYF and Nt1-222 in 20 mM tris-HCl (pH 7), 50 mM NaCl, 10 mM $MgCl_2$, 1 mM DTT, and 10% D_2O buffer at 298 K. The following experiments were recorded at 950 MHz: 2D ^{15}N-^{1}H-BEST-TROSY HSQC, 3D BEST-TROSY HNCO, 3D BEST-TROSY HNcaCO, 3D BEST-TROSY HNCA, 3D BEST-TROSY HNcoCA, 3D BEST-TROSY HNcoCACB, and 3D BEST-TROSY HNCACB (*40*). 3D BEST-TROSY hNCAnH experiment was also recorded to facilitate assignment of crowded spectrum regions corresponding to Linker resonances. Overall, 180 of 207 nonproline residues (87%) for Nt1-222 were unambiguously assigned, and chemical shift assignments have been deposited to the Biological Magnetic Resonance Bank under ID 51826. For Linker-GYF, 142 of 167 nonproline residues were assigned (85%).

NMR titrations

Series of ^{1}H,^{15}N HSQC experiments were recorded on 0.1 mM ^{15}N-labeled domains (ZnR^{GltJ}, GYF^{GltJ}, Nt1-222, or Linker-GYF^{GltJ}) upon protein or peptide partner addition. Different molar ratios were used and indicated in the corresponding figures. For GYF^{GltJ}/PRS^{AglZ} titration, the buffer was 10 mM $NaPO_4$ (pH 7). $^{1}H_2O$:$^{2}H_2O$ ratio was 90:10 (v:v). Data were obtained at 303 K.

For all other titrations, the interaction buffer was 20 mM tris-HCl (pH 7), 50 mM NaCl, 10 mM $MgCl_2$, 1 mM DTT, and 1 mM GTP or GDP. $^{1}H_2O$:$^{2}H_2O$ ratio was 90:10 (v:v). Data were obtained at 298 K.

Zn^{2+}-Cd^{2+} exchange monitored using NMR spectroscopy

Cd-EDTA solution was added to protein samples (ZnR^{GltJ}, Nt1-222, and Nt1-222 in the presence of MglA-GTP) at 2:1 molar ratio (Cd:protein). Then, 30 ^{1}H,^{15}N-HSQC experiments were recorded every 20 min to monitor Zn^{2+} replacement by Cd^{2+} ions over time.

Protein complex structure predictions

Structural prediction of MglB complexes shown in Fig. 7 was performed using AlphaFold v2.0 (*41*) in multimer mode (DB UniRef30 2302/PDB100 230517).

GAP kinetics assays

GAP accelerated GTP hydrolysis was performed using the EnzChek Phosphate Assay Kit (E-6646, Thermo Fisher Scientific). The assay is based on a method originally described by Webb (Webb, 1992). Briefly, in the presence of phosphate Pi, the substrate 2-amino-6-mercapto-7-methylpurine riboside (MESG) is converted enzymatically by purine nucleoside phosphorylase (PNP) to ribose 1-phosphate and 2-amino-6-mercapto-7-methylpurine. The assay was performed using a constant concentration of proteins (2 μM for MglA, 4 μM for MglB and MglB$^{\Delta HCt}$, and 8 μM for ZnR^{GltJ}) in a total reaction volume of 200 μl and a range of GTP concentration (0.5 to 100 μM). A master mix was prepared in buffer [50 mM tris, 10 mM NaCl, and 5 mM $MgCl_2$ (pH 7.4)] containing 1× reaction buffer, 0.2 mM MESG, and

PNP (1 U/ml). The proteins were then added, and the reaction was started by the addition of MglA. Released phosphate was recorded as the change in absorbance at 360 nm using the SPARK multimode microplate reader (Tecan) every 30 s for at least 30 min. Experiments were repeated a minimum of three times. Values for K_m and k_{cat} were calculated by fitting the data to the Michaelis-Menten equation with nonlinear regression curve fitting using GraphPad Prism (version 9.4.1, GraphPad Software Inc.).

Sequence structure and comparative genomics analyses

Sequence analysis

Previously known bona fide GYF domains were obtained from the National Center for Biotechnology Information (NCBI) Genbank database (*42*). Sequence similarity searches were performed using the PSI-BLAST (*43*) and JackHMMER (*44*) programs against the NCBI nonredundant database clustered down to 50% sequence identity using the MMseqs program (*45*). The profile-inclusion threshold was set at 0.01. Profile-profile searches were performed with the HHpred program (*46*). Alignments were constructed using the Mafft and Famsa programs, followed by refinements using HHpred profile-profile matches or HMM-align. These Multiple sequence aleignments (MSAs) were also lastly manually adjusted, guided by structure superimpositions.

Structure analysis

The JPred program (*47*) was used to predict secondary structures using MSAs (see above). Structure similarity searches were performed using the FoldSeek program (10.1101/2022.02.07.479398), and the structures were rendered, compared, and superimposed using Mol* (*48*). Structural models were generated using the RoseTTAfold program (*49*). Multiple alignments of related sequences (>30% similarity) were used to initiate HHpred searches for the step of identifying templates to be used by the neural network deployed by RoseTTAfold.

Comparative genomics

Clustering of protein sequences and the subsequent assignment of sequences to distinct families was performed by the MMseqs program. Phylogenetic analysis was performed using the rapid approximately maximum-likelihood method as implemented in the FastTree program with parameters set to: -slow (for exhaustive search); -close 0.618; -gamma -cat (set to rate categories between 5:20 based on alignment length and the Jones-Taylor-Thornton (JTT) substitution matrix (*50*). Gene neighborhoods were extracted through custom PERL scripts from genomes retrieved from the NCBI Genome database. These were then clustered using the MMseqs program and filtered using a neighborhood distance cutoff of 100 nucleotide and phyletic patterns to identify conserved gene neighborhoods.

Supplementary Materials

This PDF file includes:

Figs. S1 to S11
Tables S1 to S5
Legends for movies S1 to S9

Other Supplementary Material for this manuscript includes the following:

Movies S1 to S9

REFERENCES AND NOTES

1. M. A. Wozniak, K. Modzelewska, L. Kwong, P. J. Keely, Focal adhesion regulation of cell behavior. *Biochim. Biophys. Acta* **1692**, 103–119 (2004).
2. P. G. Charest, R. A. Firtel, Big roles for small GTPases in the control of directed cell movement. *Biochem. J.* **401**, 377–390 (2007).
3. C. De Pascalis, S. Etienne-Manneville, Single and collective cell migration: The mechanics of adhesions. *MBoC* **28**, 1833–1846 (2017).
4. L. M. Faure, J.-B. Fiche, L. Espinosa, A. Ducret, V. Anantharaman, J. Luciano, S. Lhospice, S. T. Islam, J. Tréguier, M. Sotes, E. Kuru, M. S. Van Nieuwenhze, Y. V. Brun, O. Théodoly, L. Aravind, M. Nollmann, T. Mignot, The mechanism of force transmission at bacterial focal adhesion complexes. *Nature* **539**, 530–535 (2016).
5. J. Luciano, R. Agrebi, A. V. Le Gall, M. Wartel, F. Fiegna, A. Ducret, C. Brochier-Armanet, T. Mignot, Emergence and modular evolution of a novel motility machinery in bacteria. *PLOS Genet.* **7**, e1002268 (2011).
6. B. Nan, E. M. F. Mauriello, I.-H. Sun, A. Wong, D. R. Zusman, A multi-protein complex from *Myxococcus xanthus* required for bacterial gliding motility. *Mol. Microbiol.* **76**, 1539–1554 (2010).
7. B. Nan, J. Chen, J. C. Neu, R. M. Berry, G. Oster, D. R. Zusman, Myxobacteria gliding motility requires cytoskeleton rotation powered by proton motive force. *Proc. Natl. Acad. Sci. U.S.A.* **108**, 2498–2503 (2011).
8. M. Sun, M. Wartel, E. Cascales, J. W. Shaevitz, T. Mignot, Motor-driven intracellular transport powers bacterial gliding motility. *Proc. Natl. Acad. Sci. U.S.A.* **108**, 7559–7564 (2011).
9. L. Connolley, J. Szczepaniak, C. Kleanthous, S. M. Murray, The quantitative basis for the redistribution of immobile bacterial lipoproteins to division septa. *PLOS Comput. Biol.* **17**, e1009756 (2021).
10. M. N. Webby, D. P. Williams-Jones, C. Press, C. Kleanthous, Force-generation by the trans-envelope Tol-Pal system. *Front. Microbiol.* **13**, 852176 (2022).
11. J. Szczepaniak, P. Holmes, K. Rajasekar, R. Kaminska, F. Samsudin, P. G. Inns, P. Rassam, S. Khalid, S. M. Murray, C. Redfield, C. Kleanthous, The lipoprotein Pal stabilises the bacterial outer membrane during constriction by a mobilisation-and-capture mechanism. *Nat. Commun.* **11**, 1305 (2020).
12. S. Islam, N. Jolivet, C. Cuzin, A. Belgrave, L. My, B. Fleuchot, L. Faure, U. Mahanta, A. Kezzo, F. Saidi, G. Sharma, J. B. Fiche, B. Bratton, J. Herrou, M. Nollmann, J. Shaevitz, E. Durand, T. Mignot, Unmasking of the von Willebrand A-domain surface adhesin CglB at bacterial focal adhesions mediates myxobacterial gliding motility. *Sci. Adv.* **9**, eabq0619 (2023).
13. R. Yang, S. Bartle, R. Otto, A. Stassinopoulos, M. Rogers, L. Plamann, P. Hartzell, AglZ is a filament-forming coiled-coil protein required for adventurous gliding motility of *Myxococcus xanthus*. *J. Bacteriol.* **186**, 6168–6178 (2004).
14. E. M. F. Mauriello, F. Mouhamar, B. Nan, A. Ducret, D. Dai, D. R. Zusman, T. Mignot, Bacterial motility complexes require the actin-like protein, MreB and the Ras homologue, MglA. *EMBO J.* **29**, 315–326 (2010).
15. A. Treuner-Lange, E. Macia, M. Guzzo, E. Hot, L. M. Faure, B. Jakobczak, L. Espinosa, D. Alcor, A. Ducret, D. Keilberg, J. P. Castaing, S. Lacas Gervais, M. Franco, L. Søgaard-Andersen, T. Mignot, The small G-protein MglA connects to the MreB actin cytoskeleton at bacterial focal adhesions. *J. Cell Biol.* **210**, 243–256 (2015).
16. Y. Zhang, M. Franco, A. Ducret, T. Mignot, A bacterial Ras-like small GTP-binding protein and its cognate GAP establish a dynamic spatial polarity axis to control directed motility. *PLOS Biol.* **8**, e1000430 (2010).
17. G. Fu, J. N. Bandaria, A. V. Le Gall, X. Fan, A. Yildiz, T. Mignot, D. R. Zusman, B. Nan, MotAB-like machinery drives the movement of MreB filaments during bacterial gliding motility. *Proc. Natl. Acad. Sci. U.S.A.* **115**, 2484–2489 (2018).
18. B. Nan, J. N. Bandaria, K. Y. Guo, X. Fan, A. Moghtaderi, A. Yildiz, D. R. Zusman, The polarity of myxobacterial gliding is regulated by direct interactions between the gliding motors and the Ras homolog MglA. *Proc. Natl. Acad. Sci. U. S. A.* **112**, E186–E193 (2015).
19. S. Leonardy, M. Miertzschke, I. Bulyha, E. Sperling, A. Wittinghofer, L. Søgaard-Andersen, Regulation of dynamic polarity switching in bacteria by a Ras-like G-protein and its cognate GAP. *EMBO J.* **29**, 2276–2289 (2010).
20. B. Jakobczak, D. Keilberg, K. Wuichet, L. Søgaard-Andersen, Contact- and protein transfer-dependent stimulation of assembly of the gliding motility machinery in *Myxococcus xanthus*. *PLOS Genet.* **11**, e1005341 (2015).
21. S. Balaji, L. Aravind, The RAGNYA fold: A novel fold with multiple topological variants found in functionally diverse nucleic acid, nucleotide and peptide-binding proteins. *Nucleic Acids Res.* **35**, 5658–5671 (2007).
22. M. Bergé, S. Campagne, J. Mignolet, S. Holden, L. Théraulaz, S. Manley, F. H.-T. Allain, P. H. Viollier, Modularity and determinants of a (bi-)polarization control system from free-living and obligate intracellular bacteria. *eLife* **5**, e20640 (2016).
23. M. M. Kofler, C. Freund, The GYF domain. *FEBS J.* **273**, 245–256 (2006).
24. B. Attia, B. Serrano, O. Bornet, F. Guerlesquin, L. My, J.-P. Castaing, T. Mignot, L. Elantak, ^{1}H, ^{13}C and ^{15}N chemical shift assignments of the ZnR and GYF cytoplasmic domains of the GltJ protein from *Myxococcus xanthus*. *Biomol. NMR Assign.* **16**, 219–223 (2022).
25. C. Freund, R. Kühne, H. Yang, S. Park, E. L. Reinherz, G. Wagner, Dynamic interaction of CD2 with the GYF and the SH3 domain of compartmentalized effector molecules. *EMBO J.* **21**, 5985–5995 (2002).

26. S. S. Krishna, I. Majumdar, N. V. Grishin, Structural classification of zinc fingers: Survey and summary. *Nucleic Acids Res.* **31**, 532–550 (2003).
27. D. Neuhaus, Zinc finger structure determination by NMR: Why zinc fingers can be a handful. *Prog. Nucl. Magn. Reson. Spectrosc.* **130–131**, 62 (2022).
28. J. Baranwal, S. Lhospice, M. Kanade, S. Chakraborty, P. R. Gade, S. Harne, J. Herrou, T. Mignot, P. Gayathri, Allosteric regulation of a prokaryotic small Ras-like GTPase contributes to cell polarity oscillations in bacterial motility. *PLOS Biol.* **17**, e3000459 (2019).
29. C. Galicia, S. Lhospice, P. F. Varela, S. Trapani, W. Zhang, J. Navaza, J. Herrou, T. Mignot, J. Cherfils, MglA functions as a three-state GTPase to control movement reversals of *Myxococcus xanthus*. *Nat. Commun.* **10**, 5300 (2019).
30. M. R. Webb, A continuous spectrophotometric assay for inorganic phosphate and for measuring phosphate release kinetics in biological systems. *Proc. Natl. Acad. Sci. U.S.A.* **89**, 4884–4887 (1992).
31. D. Szadkowski, A. Harms, L. A. M. Carreira, M. Wigbers, A. Potapova, K. Wuichet, D. Keilberg, U. Gerland, L. Søgaard-Andersen, Spatial control of the GTPase MglA by localized RomR-RomX GEF and MglB GAP activities enables *Myxococcus xanthus* motility. *Nat. Microbiol.* **4**, 1344–1355 (2019).
32. A. Tomar, D. D. Schlaepfer, Focal adhesion kinase: Switching between GAPs and GEFs in the regulation of cell motility. *Curr. Opin. Cell Biol.* **21**, 676–683 (2009).
33. S. Seef, J. Herrou, P. de Boissier, L. My, G. Brasseur, D. Robert, R. Jain, R. Mercier, E. Cascales, B. H. Habermann, T. Mignot, A Tad-like apparatus is required for contact-dependent prey killing in predatory social bacteria. *eLife* **10**, e72409 (2021).
34. V. H. Bustamante, I. Martínez-Flores, H. C. Vlamakis, D. R. Zusman, Analysis of the Frz signal transduction system of *Myxococcus xanthus* shows the importance of the conserved C-terminal region of the cytoplasmic chemoreceptor FrzCD in sensing signals. *Mol. Microbiol.* **53**, 1501–1513 (2004).
35. J. Schindelin, I. Arganda-Carreras, E. Frise, V. Kaynig, M. Longair, T. Pietzsch, S. Preibisch, C. Rueden, S. Saalfeld, B. Schmid, J.-Y. Tinevez, D. J. White, V. Hartenstein, K. Eliceiri, P. Tomancak, A. Cardona, Fiji: An open-source platform for biological-image analysis. *Nat. Methods* **9**, 676–682 (2012).
36. W. F. Vranken, W. Boucher, T. J. Stevens, R. H. Fogh, A. Pajon, M. Llinas, E. L. Ulrich, J. L. Markley, J. Ionides, E. D. Laue, The CCPN data model for NMR spectroscopy: Development of a software pipeline. *Proteins* **59**, 687–696 (2005).
37. Y. Shen, F. Delaglio, G. Cornilescu, A. Bax, TALOS+: A hybrid method for predicting protein backbone torsion angles from NMR chemical shifts. *J. Biomol. NMR* **44**, 213–223 (2009).
38. F. Cordier, L. Nisius, A. J. Dingley, S. Grzesiek, Direct detection of N-H[...]O=C hydrogen bonds in biomolecules by NMR spectroscopy. *Nat. Protoc.* **3**, 235–241 (2008).
39. B. Wu, J. Lukin, A. Yee, A. Lemak, A. Semesi, T. A. Ramelot, M. A. Kennedy, C. H. Arrowsmith, Solution structure of ribosomal protein L40E, a unique C4 zinc finger protein encoded by archaeon Sulfolobus solfataricus. *Protein Sci.* **17**, 589–596 (2008).
40. A. Favier, B. Brutscher, Recovering lost magnetization: Polarization enhancement in biomolecular NMR. *J. Biomol. NMR* **49**, 9–15 (2011).
41. J. Jumper, R. Evans, A. Pritzel, T. Green, M. Figurnov, O. Ronneberger, K. Tunyasuvunakool, R. Bates, A. Žídek, A. Potapenko, A. Bridgland, C. Meyer, S. A. A. Kohl, A. J. Ballard, A. Cowie, B. Romera-Paredes, S. Nikolov, R. Jain, J. Adler, T. Back, S. Petersen, D. Reiman, E. Clancy, M. Zielinski, M. Steinegger, M. Pacholska, T. Berghammer, S. Bodenstein, D. Silver, O. Vinyals, A. W. Senior, K. Kavukcuoglu, P. Kohli, D. Hassabis, Highly accurate protein structure prediction with AlphaFold. *Nature* **596**, 583–589 (2021).
42. D. A. Benson, M. Cavanaugh, K. Clark, I. Karsch-Mizrachi, D. J. Lipman, J. Ostell, E. W. Sayers, GenBank. *Nucleic Acids Res.* **41**, D36–D42 (2013).
43. S. F. Altschul, T. L. Madden, A. A. Schäffer, J. Zhang, Z. Zhang, W. Miller, D. J. Lipman, Gapped BLAST and PSI-BLAST: A new generation of protein database search programs. *Nucleic Acids Res.* **25**, 3389–3402 (1997).
44. L. S. Johnson, S. R. Eddy, E. Portugaly, Hidden Markov model speed heuristic and iterative HMM search procedure. *BMC Bioinformatics* **11**, 431 (2010).
45. M. Hauser, M. Steinegger, J. Söding, MMseqs software suite for fast and deep clustering and searching of large protein sequence sets. *Bioinformatics* **32**, 1323–1330 (2016).
46. F. Gabler, S.-Z. Nam, S. Till, M. Mirdita, M. Steinegger, J. Söding, A. N. Lupas, V. Alva, Protein sequence analysis using the MPI Bioinformatics Toolkit. *Curr. Protoc. Bioinformatics* **72**, e108 (2020).
47. A. Drozdetskiy, C. Cole, J. Procter, G. J. Barton, JPred4: A protein secondary structure prediction server. *Nucleic Acids Res.* **43**, W389–W394 (2015).
48. D. Sehnal, S. Bittrich, M. Deshpande, R. Svobodová, K. Berka, V. Bazgier, S. Velankar, S. K. Burley, J. Koča, A. S. Rose, Mol* Viewer: Modern web app for 3D visualization and analysis of large biomolecular structures. *Nucleic Acids Res.* **49**, W431–W437 (2021).
49. J. Yang, I. Anishchenko, H. Park, Z. Peng, S. Ovchinnikov, D. Baker, Improved protein structure prediction using predicted interresidue orientations. *Proc. Natl. Acad. Sci. U.S.A.* **117**, 1496–1503 (2020).
50. M. N. Price, P. S. Dehal, A. P. Arkin, FastTree 2 – Approximately maximum-likelihood trees for large alignments. *PLOS ONE* **5**, e9490 (2010).

Acknowledgments: We thank F. Guerlesquin for discussions and D. Byrne for technical assistance during ITC experiments. Language and readability were improved with the assistance of generative AI (Chat-GPT 3.5). Financial support from the IR INFRANALYTICS FR2054 for conducting the research is acknowledged. **Funding:** This work was supported by Intramural Funds of the National Library of Medicine, USA (to L.A. and V.A.). J.P.C. was supported by a Fondation Bettencourt Schueller "coup d'élan pour la recherche française" to T.M., and C.D. was supported by a CENTURI Post-doc fellowship and an ERC-Advanced grant (JAWS) to T.M. **Author contributions:** Conceptualization: B.A., L.M., J.P.C., P.V., L.El., and T.M. Methodology: B.A., L.M., C.D., H.L.G., L.Es., L.El., M.N., V.A., L.A., O.B., C.S.-K., and T.M. Investigation: B.A., L.M., J.P.C., C.D., V.S., V.A., and L.A. Visualization: L.Es., H.L.G., V.A., and L.A. Funding acquisition: L.El. and T.M. Supervision: L.El. and T.M. Writing—original draft: L.El. and T.M. Writing—review and editing: B.A., L.M., L.El., and T.M. **Competing interests:** The authors declare that they have no competing interests. **Data and materials availability:** Structures of the free ZnR^{GltJ} and GYF^{GltJ} domains were deposited in the Protein Data Bank (PDB) database with the accession codes: 7Z0K and 7Z3C, respectively. All the other data needed to evaluate the conclusions in the paper are present in the paper and/or the Supplementary Materials.

Submitted 1 December 2023
Accepted 23 April 2024
Published 29 May 2024
10.1126/sciadv.adn2789